

The Solid Solution - Aqueous Solution System (Sr,Ba,Ra)SO₄ + H₂O: A Combined Experimental and Theoretical Study of Phase Equilibria at Sr-rich Compositions

Authors

Martina Klinkenberg^{1*}, Juliane Weber^{1,†}, Juri Barthel^{2,3}, Victor Vinograd¹, Jenna Poonosamy¹, Maximilian Kruth^{2,3}, Dirk Bosbach¹, Felix Brandt¹

¹Institute of Energy and Climate Research (IEK-6) – Nuclear Waste Management and Reactor Safety, Forschungszentrum Jülich GmbH, 52425 Jülich, Germany

²Central Facility for Electron Microscopy, (GFE), RWTH Aachen University, 52074 Aachen, Germany

³Ernst Ruska-Centre for Microscopy and Spectroscopy with Electrons, Forschungszentrum Jülich GmbH, 52425 Jülich, Germany

Abstract

Solid solution formation between RaSO₄ and other isostructural sulfates has been known for a long time as a process potentially controlling Ra concentrations in aquifers. Here, we measured the Ra uptake in the Sr-rich corner of the ternary (Sr,Ba,Ra)SO₄ solid solution - aqueous solution (SS-AS) system by equilibrating SrSO₄, BaSO₄ and mixed (Sr,Ba)SO₄ solids with Ra-bearing aqueous solutions for up to 1302 days at 90 °C at a solid/liquid ratio of 5 g/L. The recrystallization experiments were combined with electron microscopy studies of the solids. The evolution of the solid and aqueous phases was interpreted based on thermodynamic modelling applying a recently revised thermodynamic dataset for the (Sr,Ba,Ra)SO₄ + H₂O system.

The recrystallization process involved several metastable phases, starting from the least soluble, Ba- and Ra-rich precipitates and ending with Sr-rich solids, whose compositions approached the predicted equilibrium states. The composition and the time evolution of metastable phases were correlated with changes in the computed supersaturation functions. Particularly, the formation of Ra-Ba- and Sr-rich rims on primary barite grains in the experiment with the mechanical mixture of 99 %

* E-mail of corresponding author: m.klinkenberg@fz-juelich.de, Tel.: +49 2461 61- 3779

† Present address: Chemical Science Division, Oak Ridge National Laboratory, USA.

of celestine and 1 % of barite has been explained by combining calculated supersaturation conditions with considerations of structural misfit.

A key result was the observed final Ra_{aq} concentration which is about one order of magnitude lower compared to the initial concentration, implying an efficient uptake into the newly formed solid phases. These concentrations appeared to be just slightly lower than those predicted by the thermodynamic calculations, implying that the complete SS-AS equilibrium was close to be reached in Sr-rich systems in the recrystallization experiments lasting for about 3.5 years.

Highlights

- Formation and evolution of the ternary (Sr,Ba,Ra)SO₄ solid solution
- Intermediate, Ra-rich phases observed by FIB, SEM, TEM indicate a complex recrystallization process involving several metastable states
- Metastable states and approach to equilibrium are explained based on a recent thermodynamic model and supersaturation calculations
- The ternary (Sr,Ba,Ra)SO₄ offers a potential for efficient Ra retention, reducing the Ra-concentration in aqueous solution by one order of magnitude

Key words

radium uptake, recrystallization, (Sr,Ba,Ra)SO₄ solid solution, barite, celestine, ternary solid solution thermodynamics

1 Introduction

Direct disposal of spent nuclear fuel in deep geological formations is currently considered as the best option for closing the nuclear energy cycle (SKB, 2011; Nagra, 2014, Ewing et al., 2016). The long-term safety of an underground repository can be assessed theoretically through the consideration of the fate of important radionuclides in various geochemical scenarios, including those, where the waste is allowed to come into contact with ground waters. An adequate and accurate thermodynamic data base is required for the safety assessment. For example, ²²⁶Ra becomes a main contributor to the

total dose after about $10^4 - 10^5$ years of waste disposal (SKB, 2011). Many recent studies agree in the conclusion that the release of ^{226}Ra from the waste into an aquifer will be controlled by solid-aqueous equilibria involving barite-type solid solutions (Kulik et al., 2004; Bruno et al. 2007; Grandia et al., 2008) and will be very limited, due to the tendency of Ra to partition into the solid phase. The thermodynamic properties of the ternary solid solution - aqueous solution (SS-AS) system $(\text{Sr},\text{Ba},\text{Ra})\text{SO}_4 + \text{H}_2\text{O}$, which are required for a quantitative analysis of the Ra retention by barite, have been recently refined based on an extensive set of first-principles-based atomistic simulations (Vinograd et al., 2013; 2018a,b).

While previous experimental works have been mostly focused on the binary sub-system $(\text{Ba},\text{Ra})\text{SO}_4 + \text{H}_2\text{O}$ (Bosbach et al., 2010; Curti et al., 2010; Klinkenberg et al., 2014; Brandt et al., 2015; Weber et al., 2017; Heberling et al., 2018), we investigated here Sr-rich compositions of the ternary SS-AS system within experiments lasting for more than 3 years. Main targets of the present study are to test (i) the feasibility of attaining the thermodynamic equilibrium in such experiments and (ii) the accuracy of a recently revised thermodynamic dataset for the $(\text{Sr},\text{Ba},\text{Ra})\text{SO}_4$ system (Vinograd et al. 2018b). For this purpose the Ra uptake is measured with time in batch experiments of different initial solid-phase composition and microstructure, including mechanical mixtures of pure barite and pure celestine as well as pre-synthesized homogeneous solid solutions.

The macroscopic experimental approach was combined with microscopy (scanning and transmission electron microscopy (SEM, TEM), focused ion beam (FIB)) and thermodynamic modelling to achieve a better understanding of the Ra uptake mechanisms into ternary, Sr-rich compositions. The first principles based modelling study of the ternary solid solution (Vinograd et al., 2018a) has shown that the non-ideality in the binaries increases in the row of Ba-Ra, Ba-Sr and Sr-Ra, such that the $(\text{Ba},\text{Ra})\text{SO}_4$ solid solution is fully miscible at all temperatures of interest, the $(\text{Ba},\text{Sr})\text{SO}_4$ solid solution starts to decompose at about 300 K, while only very limited mixing exists in the $(\text{Sr},\text{Ra})\text{SO}_4$ solid solution at all temperatures. A combination of these binary mixing tendencies at ~ 300 K corresponds to a wide ternary miscibility gap, which opens at the Sr-Ra binary and closes at the Ba-Sr binary. The shape of this gap at ambient temperatures has been described applying the ternary regular mixing model with the parameters $W_{\text{BaRa}} = 2.47 \pm 0.22$ kJ/mol,

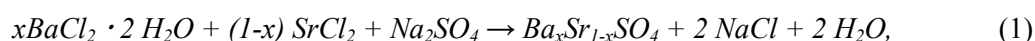
$W_{\text{BaSr}} = 4.95 \pm 0.75$ kJ/mol and $W_{\text{SrRa}} = 17.5 \pm 1.40$ kJ/mol. These results suggested that Ra-uptake at Sr-rich compositions would be less efficient relative to that of pure barite due to a much higher value of the activity coefficient of RaSO_4 , which at $x_{\text{Sr}} \sim 1$ is mostly determined by the large value of W_{SrRa} . This prediction is tested in the present study.

The study of Vinograd et al. (2018a) predicted that Sr-rich and moderately Ra-rich ternary compositions should decompose into a major Sr-rich celestine phase and a minor phase, which is simultaneously rich in Ba and Ra. The Ra/Ba ratio in the latter phase was predicted to rapidly increase with the SrSO_4 -content in the system. In order to test this working hypothesis and to help the system to develop the relevant phase separation, some starting compositions in our experiments were composed of a mechanical mixture of barite and celestine powders with 1 % fraction of barite grains. We expected to observe the growth of a $(\text{Ba,Ra})\text{SO}_4$ solid solution on top of the barite seeds and to measure its composition with SEM-EDX. We were also interested in studying the situation, where the starting material was a single-phase homogeneous Sr-rich $(\text{Sr,Ba})\text{SO}_4$ solid solution. In this case a phase separation was expected to be possible. By sampling tiny portions of the reacted solids and aliquots of the aqueous solution at well-defined time intervals, we observed various re-crystallization phenomena at intermediate stages of the system equilibration and related them to the evolution of the supersaturation of the aqueous phase.

2 Materials and Methods

2.1. Synthesis and characterization of $BaSO_4$, $SrSO_4$, and $(Ba,Sr)SO_4$ solid solutions

Homogeneous solid solutions with a defined composition were synthesized by the flux method. Pure endmembers synthesis ($BaSO_4$ and $SrSO_4$) was based on procedures by Patel & Koshy (1968) and Patel & Bhat (1971). Stoichiometric mixtures of Na_2SO_4 and $BaCl_2 \cdot H_2O$ or $SrCl_2$ respectively, were heated above their melting point to react to $BaSO_4$ or $SrSO_4$ and afterwards cooled down in several steps. The synthesis of $(Ba_{1-x}Sr_x)SO_4$ solid solutions followed equation (1)



where x is the mole fraction of $BaSO_4$ in the solid solution. The chemicals were ground, weighed, mixed and ground again. The reactants were heated above 1000 °C and cooled to room temperature in platinum crucibles. Afterwards the melt cake was washed with deionized water to remove the NaCl. A grain size fraction of 20 – 63 µm was separated by grinding and sieving. Samples were embedded in epoxy and polished for electron microprobe (EMP) analyses. The compositions of the synthesized samples are given in Table 1.

Table 1 Overview of solids synthesized by the flux method.

	X_{BaSO_4}	X_{SrSO_4}
$BaSO_4$	1.00	0.00
$SrSO_4$	0.00	1.00
$(Ba_{0.01}Sr_{0.99})SO_4$	$0.008 \pm 10 \%$	0.992
$(Ba_{0.03}Sr_{0.97})SO_4$	$0.03 \pm 10 \%$	0.97

The chemical composition and homogeneity of the synthesized solids were analyzed by EMP with a JEOL 8200 Superprobe equipped with a tungsten hair pin cathode. The used standards and analyzed lines for each element are summarized in the supplementary materials (Table S1). Samples and standards were measured with a spot size of 10 µm, an acceleration voltage of 15 kV and an emission current of $1.5 \cdot 10^{-8}$ A. The EMP analyses indicated homogeneous chemical compositions of synthesized crystals suitable for the planned batch experiments.

2.2. Sample preparation and experimental setup

We synthesized solid solutions and pure endmembers by the flux method in this study, in contrast to previous studies (Curti et al. 2010, Klinkenberg et al. 2014, Brandt et al. 2015, Weber et al. 2017, Vinograd et al. 2018, Heberling et al., 2018) where barite samples from a precipitation route were used. The advantage of synthesis by the flux method is that it allows for obtaining homogenous solid solutions, while the precipitated solids may have inhomogeneous compositions, zoning, trapped fluid inclusions or other defects. In order to compare the present experiments with our earlier experiments (Vinograd et al. 2018b), a sample of pure barite from flux synthesis was re-crystallized in the Ra-bearing aqueous solution. The results were compared to those from the experiments with *Sachtleben* and *Aldrich* barites synthesized by precipitation described in Vinograd et al. 2018b (S/L = 5 g/L, 90 °C).

The general batch experiment setup was adapted from earlier studies (e.g. Brandt et al., 2015, Klinkenberg et al., 2014). The uptake of Ra was observed, starting from a concentration of $5.0 \cdot 10^{-6}$ mol/L in all experiments and 0.1 mol/L of NaCl as background electrolyte. The experiments were performed at 90 °C with a solid/liquid ratio of 5 g/L. Eight batch recrystallization experiments were carried out for 1302 days (the working names of the experimental runs are given in italics):

1. *reference barite*: pure barite (Fig. 1 a) in Ra-free aqueous solution
2. *barite*: pure barite in Ra-bearing aqueous solution
3. *reference celestine 99 + barite 1*: mechanical mixture of 99 mol% celestine and 1 mol% barite (Fig. 1 b) in Ra-free aqueous solution
4. *celestine 99 + barite 1*: mechanical mixture of 99 mol% celestine and 1 mol% barite in Ra-bearing aqueous solution
5. *reference (Ba_{0.01}Sr_{0.99})SO₄*: solid solution of 99 mol% SrSO₄ and 1 mol% BaSO₄ (Fig. 1 c) in Ra-free aqueous solution
6. *(Ba_{0.01}Sr_{0.99})SO₄*: solid solution of 99 mol% SrSO₄ and 1 mol% BaSO₄ in Ra-bearing aqueous solution
7. *reference (Ba_{0.03}Sr_{0.97})SO₄*: solid solution of 97 mol% SrSO₄ and 3 mol% BaSO₄ in Ra-free aqueous solution

8. $(\text{Ba}_{0.03}\text{Sr}_{0.97})\text{SO}_4$ solid solution of 97 mol% SrSO_4 and 3 mol% BaSO_4 in Ra-bearing aqueous solution

The initial morphology of the grains in all experiments was dominated by fractured or cleaved surfaces. Some grains exhibited conchoidal fractures.

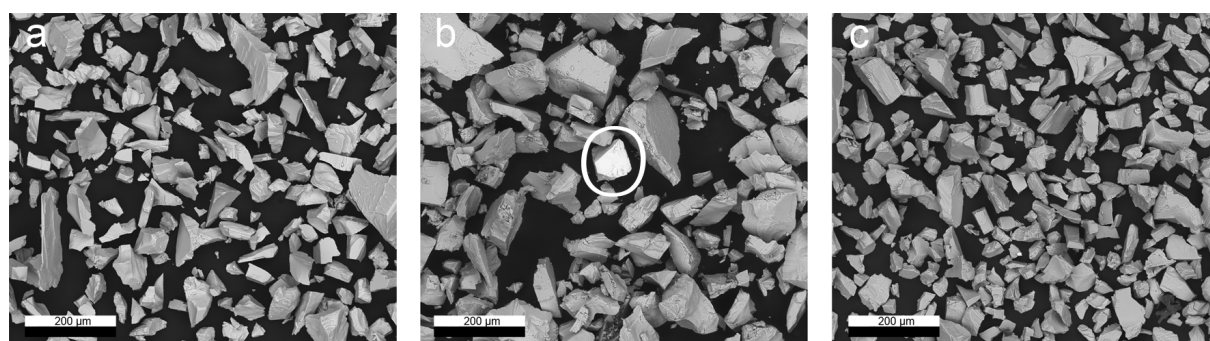


Fig. 1. SEM images of a) pure barite, b) mechanical mixture of 99 % celestine and 1 % barite (the bright barite grain is highlighted in the middle) c) $(\text{Ba}_{0.01}\text{Sr}_{0.99})\text{SO}_4$ solid solution after grain size separation.

2.2.1 Sampling and analysis of the aqueous phase in the batch experiments

The sampling and analysis procedure of the aqueous phase was the same as in Klinkenberg et al. (2014). Further details are provided in the supplementary materials.

2.3. Sampling and the analysis of the solids

2.3.1 Scanning electron microscopy (SEM) and energy dispersive x-ray spectrometry (EDS)

Small amounts of solids were sampled during the recrystallization experiments. The evolution of the crystal morphology and chemical composition was studied using the environmental scanning electron microscope FEI Quanta 200 F combined with energy dispersive X-ray spectrometry (EDS, EDAX). In order to avoid artefacts due to precipitation of NaCl , SrSO_4 or RaSO_4 , the samples were cleaned by two washing steps in isopropanol. The samples were then prepared as suspensions on Cu or Si holders and subsequently dried.

2.3.2 Preparation of thin lamellae by focused ion beam (FIB)

A ~ 100 nm thick cross-section lamella was cut out of a barite grain from the experiment celestine 99 + barite 1, day 226 by utilizing a NVision 40 cross beam station (Carl Zeiss AG, Germany). A detailed description of the procedure is given in Weber et al. 2016.

2.3.3 Transmission Electron Microscopy (TEM)

The thin cross-section lamella was investigated using several TEM techniques with a FEI Tecnai G² F20 (Thermo Fischer Scientific, The Netherlands) operated at 200 kV accelerating voltage (Luysberg, M. et al., 2016). High-angle annular dark-field (HAADF) images were recorded in scanning transmission electron microscopy (STEM) mode realizing Z-contrast imaging of the thin cross section (Pennycook, S., 1989). In our STEM experiments the electron probe was formed with 12 mrad convergence semi-angle, and the intensities of diffracted beams were recorded with an annular detector covering the angular range of 85 mrad up to about 200 mrad in a magnified image of the back-focal plane. In this HAADF setup, the recorded intensity increases with increasing accumulated atomic core charge at the position of the small scanning probe. Higher intensity indicates a composition with higher atomic number, larger sample thickness, or higher material density. In the present context, intensity variations are expected due to changes in composition between elements of high and low atomic numbers: Ra ($Z = 88$), Ba ($Z = 56$), and Sr ($Z = 38$). The HAADF STEM imaging was therefore complemented with EDS mapping.

2.4. Thermodynamics of mixing in the ternary system (Sr,Ba,Ra)SO₄

The study of Vinograd et al. (2018a) recommended the regular model description of the ternary solid solution with the parameters $W_{\text{BaRa}} = 2.47 \pm 0.22$ kJ/mol, $W_{\text{BaSr}} = 4.95 \pm 0.75$ kJ/mol and $W_{\text{SrRa}} = 17.5 \pm 1.40$ kJ/mol. The simple three-parameter regular equation has been obtained, however, at the cost of a less accurate description of mixing in the dilute limits of $x_{\text{Ba}} \sim 1$ and $x_{\text{Sr}} \sim 1$. Indeed, the Margules parameter $W_{\text{BaSr}} = 4.95$ kJ/mol was set to model the lowering of the free energy in the intermediate range of compositions in the system of Ba-Sr, which is driven by short range order (SRO). However, SRO vanishes in dilute limits, i.e. at high BaSO₄ or high SrSO₄ concentrations.

Thus, the best model for these compositions should exclude the effect of SRO. The calculations of Vinograd et al., 2013 and Vinograd et al., 2018a based on the single defect method showed that the dilute limits of the (Ba,Sr)SO₄ solid solution are well described with the interaction parameter $W_{\text{BaSr}} = 8.34 \pm 0.60$ kJ/mol. Similarly, at the Sr-rich compositions the (Sr,Ra)SO₄ solid solution is well described with the interaction parameter $W_{\text{SrRa}} = 19.80 \pm 0.60$ kJ/mol.

As the majority of the experimental data of the present study refer to very Sr-rich and Ba- and Ra-poor compositions, the latter parameter values should be preferred. Thus, the modelling of the equilibrium states at Sr-rich compositions has been performed here with the regular ternary model, in which the parameters W_{BaSr} and W_{SrRa} were 8.34 kJ/mol and 19.8 kJ/mol, respectively.

A more accurate description of the binary Ba-Sr solid solution at ambient temperatures covering the whole range of the compositions can be obtained with a spline model, which envelopes two regular models, such that the enthalpy of mixing coincides with the regular model equations constrained by the parameters $W_0 = 8.34$ kJ/mol and $W_{0.5} = 4.95$ kJ/mol in the dilute and intermediate compositions, respectively. The spline equation (1) can be written as

$$H_{\text{mix}} = x(1-x)(16(W_0 - W_{0.5})(x-0.5)^4 + W_{0.5}) \quad (1)$$

where x is the mole fraction of celestine. In Fig. 2 this function is plotted as the solid line.

The activity coefficients of BaSO₄ and SrSO₄, which correspond to the spline model are given by the following equations

$$RT \ln \gamma_{\text{SrSO}_4} = W_{0.5}(1-x)^2 + (W_0 - W_{0.5})(1-x)^2(80x^4 - 128x^3 + 72x^2 - 16x + 1) \quad (2)$$

and

$$RT \ln \gamma_{\text{BaSO}_4} = W_{0.5}x^2 + (W_0 - W_{0.5})x^2(80x^4 - 192x^3 + 168x^2 - 64x + 9), \quad (3)$$

where x is the mole fraction of celestine. The last two equations were used here to compute saturation states in Ra-free experiments. Although the spline model is given by a mathematically very simple equation for the (Ba,Sr)SO₄ binary, there is still a difficulty of implementing it directly into the GEM-Selektor software package (GEMS, <http://gems.web.psi.ch>) to model the ternary solid solution. Thus, in the present modelling study two separate ternary regular models with the parameters $W_{\text{BaRa}} = 2.47$ kJ/mol, $W_{\text{BaSr}} = 4.95$ kJ/mol, $W_{\text{SrRa}} = 17.5$ kJ/mol and $W_{\text{BaRa}} = 2.47$ kJ/mol, $W_{\text{BaSr}} = 8.34$ kJ/mol $W_{\text{SrRa}} = 19.8$ kJ/mol were used. The first model was implemented in the

calculations of saturation states relative to the ternary solid solution, to explain the formation of the ternary intermediate Ba- and Ra-rich intermediate phase, while the second model was used to compute final equilibrium states, in which the formation of stable dilute solid solutions was expected.

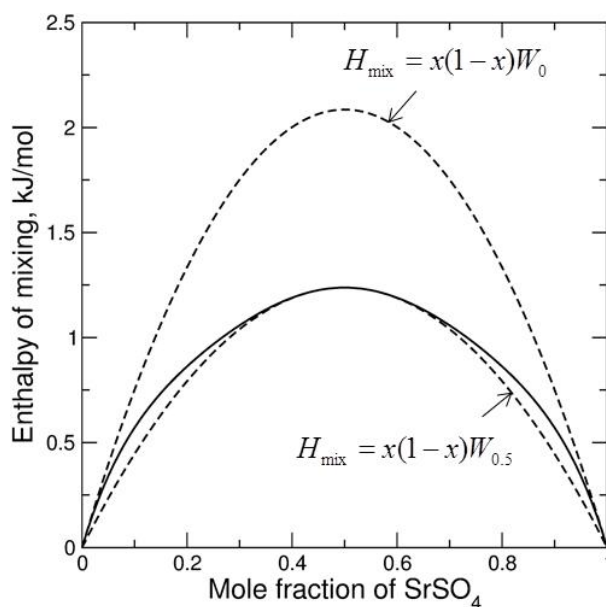


Fig. 2. The spline model of the binary (Ba,Sr)SO₄ solid solution corresponding to the parameters $W_0 = 8.34$ kJ/mol and $W_{0.5} = 4.95$ kJ/mol. The latter parameters define two regular mixing models, which are valid at the dilute and at intermediate compositions, respectively. The regular model enthalpies are shown as dashed lines.

2.5. Modelling of solid aqueous equilibria and evaluation of metastable conditions

Gibbs energy minimization approaches implemented in the GEMS3K solver (<http://gems.web.psi.ch/GEMS3K>) and described in Kulik et al. (2013) were used to calculate the solid solution composition as well as the aqueous solution equilibria at 90 °C. The activity coefficients for all dissolved species were calculated according to the extended Debye-Hückel model (Helgeson et al. 1981, Johnson et al., 1992). The application of this model, of which a detailed description is provided in Wagner et al. (2012), is justified by the relatively low ionic strength of the solution at equilibrium (ionic strength ~ 0.1). Thermodynamic data for aqueous species were taken from the PSI-Nagra database (Thoenen et al., 2014) integrated in GEMS that inherits temperature and pressure

dependencies for most aqueous ions and complexes from the HKF EoS (Helgeson et al., 1981) as given in the SUPCRT92 database (<http://gems.web.psi.ch/TDB>).

Although only certain defined compositions of a solid solution could coexist at the thermodynamic equilibrium with the aqueous phase, at non-equilibrium a wide range of solid solution compositions can precipitate from the same aqueous solution (Prieto et al. 1993; Pina et al., 2000). These non-equilibrium precipitates can occur at the early stages of the experiments. The most likely compositions correspond to the maximum value of the supersaturation Ω , which is defined for a pure system, e.g. BaSO₄ as:

$$\Omega_{barite} = \frac{a(\text{Ba}^{2+}) a(\text{SO}_4^{2-})}{K_{(\text{BaSO}_4)}} \quad (4)$$

where $a(\text{Ba}^{2+})$ and $a(\text{SO}_4^{2-})$ represent the activities of the aqueous species and $K_{(\text{BaSO}_4)}$ is the solubility product of BaSO₄. In a SS-AS system, the supersaturation of an aqueous solution is not a unique value, but rather a function of the composition of the solid phase. The supersaturation relative to the binary (Sr,Ba)SO₄ solid solution can be computed as follows (Prieto et al. (1991):

$$\Omega_{(\text{Sr,Ba})\text{SO}_4} = \frac{a(\text{Sr}^{2+})^{x_{\text{Sr}}} a(\text{Ba}^{2+})^{x_{\text{Ba}}} a(\text{SO}_4^{2-})}{(x_{\text{Sr}} \gamma_{\text{Sr}} K_{(\text{SrSO}_4)})^{x_{\text{Sr}}} (x_{\text{Ba}} \gamma_{\text{Ba}} K_{(\text{BaSO}_4)})^{x_{\text{Ba}}}} \quad (5)$$

where $a(\text{Ba}^{2+})$, $a(\text{Sr}^{2+})$ and $a(\text{SO}_4^{2-})$ represent the activities of the ions in the aqueous solution; $K_{(\text{BaSO}_4)}$, and $K_{(\text{SrSO}_4)}$ are the solubility products of the end-members BaSO₄, and SrSO₄ at the temperature of interest; x_{Ba} , and x_{Sr} are the mole fractions of BaSO₄ and SrSO₄ in the solid and γ_{Ba} and γ_{Sr} are the activity coefficients of the end members. The last equation can be easily generalized for the case of the ternary (Sr,Ba,Ra)SO₄ system:

$$\Omega_{(\text{Sr,Ba,Ra})\text{SO}_4} = \frac{a(\text{Sr}^{2+})^{x_{\text{Sr}}} a(\text{Ra}^{2+})^{x_{\text{Ra}}} a(\text{Ba}^{2+})^{x_{\text{Ba}}} a(\text{SO}_4^{2-})}{(x_{\text{Sr}} \gamma_{\text{Sr}} K_{(\text{SrSO}_4)})^{x_{\text{Sr}}} (x_{\text{Ra}} \gamma_{\text{Ra}} K_{(\text{RaSO}_4)})^{x_{\text{Ra}}} (x_{\text{Ba}} \gamma_{\text{Ba}} K_{(\text{BaSO}_4)})^{x_{\text{Ba}}}} \quad (6)$$

where the additional parameters refer to the Ra-bearing species and end members. Equilibrium corresponds to $\Omega = 1$. For $\Omega < 1$ dissolution can occur, whereas for $\Omega > 1$ precipitation can take place. The solubility products of BaSO₄ and SrSO₄ ($K_{(\text{BaSO}_4)}^0 = 10^{-9.97}$ and $K_{(\text{SrSO}_4)}^0 = 10^{-6.63}$) at the standard temperature were taken from Hummel et al. (2002) and that of RaSO₄ ($K_{(\text{RaSO}_4)}^0 = 10^{-10.26}$) from Langmuir and Riese, 1985). The solubility products $K_{(\text{BaSO}_4)}$, $K_{(\text{RaSO}_4)}$, $K_{(\text{SrSO}_4)}$ at 90 °C were calculated using the GEMS ‘RTplot’ Tool database with temperature and pressure dependencies for the aqueous

ions and complexes accounted by the HKF EoS (Helgeson et al., 1981) and the C_p functions for the solids summarized in Vinograd et al. (2018b). The solubility products at 90 °C used in our supersaturation calculations (equations 5 and 6) are $K(T)_{(\text{BaSO}_4)} = 10^{-9.55}$, $K(T)_{(\text{SrSO}_4)} = 10^{-7.1}$ and $K(T)_{(\text{RaSO}_4)} = 10^{-10.55}$. For the binary solid solution (Ba,Sr)SO₄, the activities of the solid, γ , are calculated for the BaSO₄ and SrSO₄ end members following equation 2 and 3 respectively. For the ternary solid solution (Sr,Ba,Ra)SO₄, the activities coefficients of the respective endmembers within the solid were calculated assuming the regular mixing model with zero ternary interaction parameter as described in Wagner et al. 2012.

2.6. Structural misfit

Best conditions for epitaxial growth occur when the unit cell dimensions of a newly formed precipitate are equal to the unit cell dimensions of the substrate. The relative easiness/difficulty of the epitaxial growth for a solid solution of a given composition on a seed of pure barite can be related to the following misfit function

$$Q = \sum_{i=1}^3 (a_{ss,i} - a_{Ba,i})^2, \quad (7)$$

where $a_{ss,i}$ and $a_{Ba,i}$ are the cell parameters of the solid solution and barite, respectively. The cell parameters of a solid solution with the composition defined by the mole fractions of x_{Ba} , x_{Sr} , and x_{Ra} of barite, celestine and RaSO₄, respectively, were computed with the equation

$$a_{ss,i} = x_{\text{Ba}} a_{\text{Ba},i} + x_{\text{Sr}} a_{\text{Sr},i} + x_{\text{Ra}} a_{\text{Ra},i}, \quad (8)$$

where $a_{\text{Ba},i}$, $a_{\text{Sr},i}$ and $a_{\text{Ra},i}$ are the corresponding unit cell parameters of pure barite, celestine and RaSO₄, respectively. The cell parameters of barite and celestine were taken from Jacobsen et al. (1998), the data for RaSO₄ from Weigel and Trinkl (1968). As the unit cell parameters of celestine and RaSO₄ are, respectively, smaller and larger, than the parameters of barite, there exist a continuity of ternary solid solution compositions, which are characterized by zero Q value, i.e. zero misfit relative to pure barite.

3 Results and Discussion

In the following, we present the results of the batch experiments beginning with the temporal evolution of the cation concentrations measured in the aqueous solution at selected times up to 3.5 years. Electron microscopy of simultaneously extracted solid samples accompanies these results, indicating that differences in the solution dynamics are related to differences in the microstructural evolution of the solids. Most of these observations can be explained by the thermodynamic modelling, which provides a basis for discussing the temporal evolution of the system in great detail. A few remaining discrepancies between experiment and theory are discussed and may be related to small inaccuracies in the modelling as well as insufficient equilibration of the experiment.

3.1. Temporal evolution of the Ra, Ba, and Sr concentrations in the aqueous solution

The Ra_{aq} concentration in the presence of pure barite showed a significant decrease within the first 70 days of the experiment and reached a plateau of $1.5 \cdot 10^{-8}$ mol/L after 200 days. In the course of this experiment the initial Ra_{aq} concentration decreased by 99.75 % (Fig. 3 a). Both, the final Ra_{aq} concentration as well as the temporal evolution are in very good agreement with those observed by Vinograd et al. 2018b in their experiments ($S/L = 5$ g/L, 90°C) with *Sachtleben* and *Aldrich* barite (Fig. 3 a). Those experiments showed a final Ra_{aq} concentration of $1 \cdot 10^{-8}$ - $2 \cdot 10^{-8}$ mol/L. In the presence of Ra, the Ba_{aq} concentration in the experiment with barite from flux synthesis quickly stabilized at $4 \cdot 10^{-5}$ mol/L (Fig. 3 d), similar to $5 \cdot 10^{-5}$ mol/L observed in the reference experiment without Ra (Fig. 3 g).

In the experiment with the mechanical mixture *celestine 99* + *barite 1*, the temporal evolution of the Ra_{aq} concentration indicated a stepwise recrystallization: the first minimum at $2 \cdot 10^{-6}$ mol/L was observed after 30 days, then the concentration increased to $3.5 \cdot 10^{-6}$ mol/L, and dropped after 226 days to a plateau of $1 \cdot 10^{-7}$ mol/L after ~ 600 days (Fig. 3 b). The concentration of Ba_{aq} rose in the beginning to $1 \cdot 10^{-5}$ mol/L (Fig. 3 e), and after 100 days reached a plateau at $3 \cdot 10^{-6}$ mol/L. On the contrary, in the reference experiments without Ra (Fig. 3 h), the Ba_{aq} concentration initially stayed at $1 \cdot 10^{-6}$ mol/L, i.e. one order of a magnitude lower compared to the experiment with Ra, and then after 100 days increased reaching a plateau of

2 · 10⁻⁶ mol/L. The concentration of Sr_{aq} remained stable (1 · 10⁻³ mol/L) in both experiments, independent of the presence of Ra (Fig. S1 a).

The temporal evolution of the total metal concentrations in the experiments with solid solutions of (Ba_{0.01}Sr_{0.99})SO₄ and (Ba_{0.03}Sr_{0.97})SO₄ is similar to that of the experiments starting from the mechanical mixture *celestine 99 + barite 1*. At the beginning, the Ra_{aq} concentration dropped down to the first minimum of 1 - 2 · 10⁻⁶ mol/L. Then after ~ 40 days the Ra_{aq} concentration reached the maximum of 2.5 – 3 · 10⁻⁶ mol/L and then slowly decreased reaching a plateau at 1.5 · 10⁻⁷ mol/L after ~ 600 days (Fig. 3 c). The Ba_{aq} concentration elevated to 8.5 · 10⁻⁶ mol/L at the beginning of the experiment with Ra and after 100 days, reached plateau values of ca. 2 · 10⁻⁶ mol/L in the case of (Ba_{0.01}Sr_{0.99})SO₄ and 4 · 10⁻⁶ mol/L in the case of (Ba_{0.03}Sr_{0.97})SO₄ (Fig. 3 f).

The temporal evolution of the Ba_{aq} concentration is similar in Ra-free reference and Ra-containing experiments (Fig. 3 i). First, the concentration of Ba_{aq} rose to ~ 9 · 10⁻⁶ mol/L and then reached the plateau values of 2 · 10⁻⁶ mol/L in the case of *reference* (Ba_{0.01}Sr_{0.99})SO₄ and 4 · 10⁻⁶ mol/L in the case of *reference* (Ba_{0.03}Sr_{0.97})SO₄ after 100 days. The concentration of Sr_{aq} remained stable at 1 · 10⁻³ mol/L in both experiments as well as in reference experiments without Ra (Fig. S1 b). All the experimental results of the aqueous metal concentrations are summarized in Table A.1 - Table A.5 of the appendix.

In summary of the macroscopic results, all experiments showed a significant decrease of Ra_{aq} of at least one order of magnitude after 1302 days. For the binary SS-AS system with pure barite and Ra in the aqueous solution, a continuous decrease of the Ra_{aq} concentration was observed. On the contrary, the experiments in the ternary SS-AS system with the mechanical mixture and the solid solutions showed a fluctuation of the Ra_{aq} concentration within the first year. Differences were also observed in the evolution of the Ba_{aq} concentrations, where a constant Ba_{aq} concentration for pure barite and a decrease of the Ba_{aq} concentrations in the ternary SS-SA system was observed. The results of cation metal concentrations are discussed and compared to the thermodynamically predicted values in section 3.3.

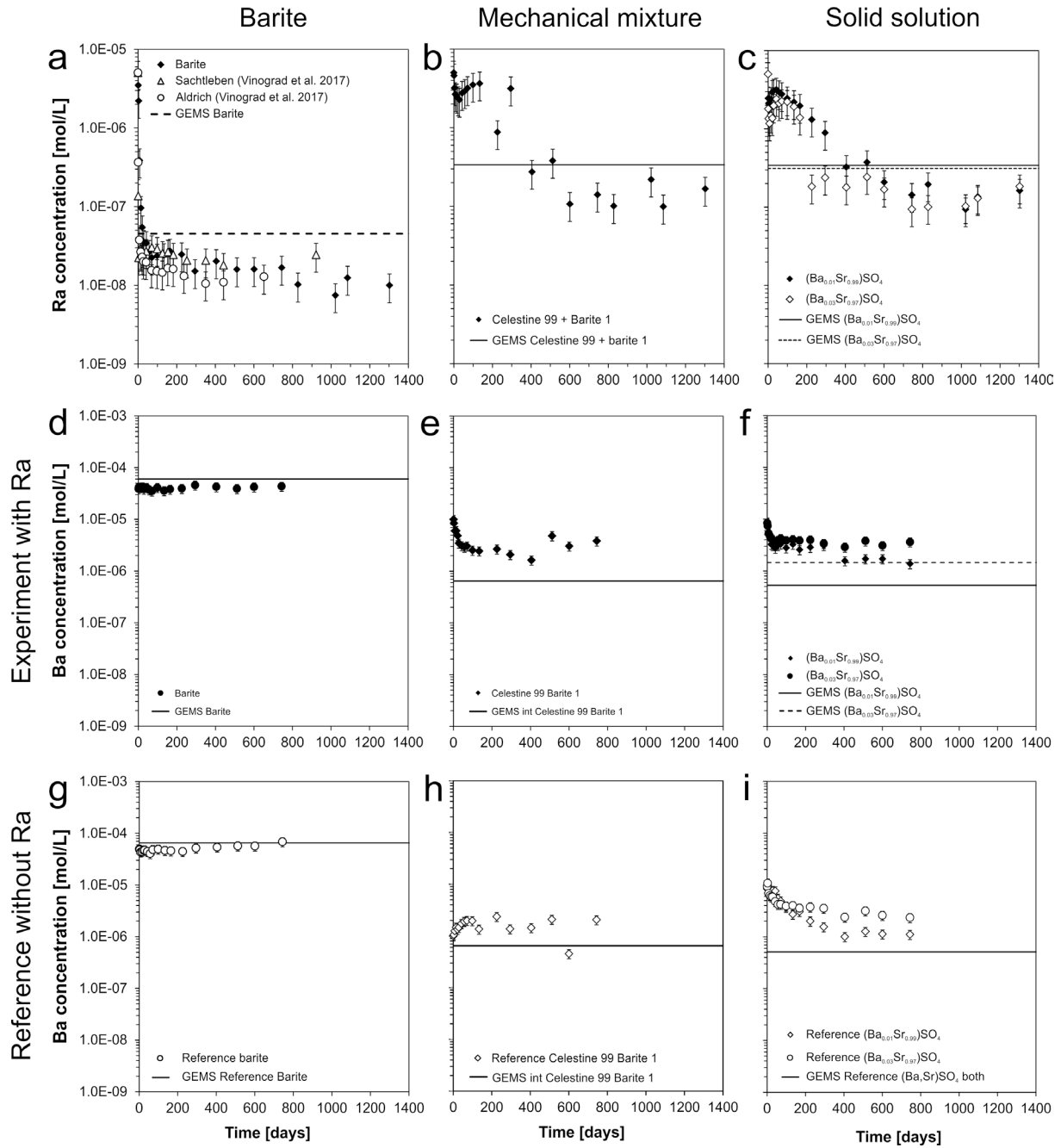


Fig. 3. Temporal evolution of the Ra_{aq} concentrations a) of pure *barite* (flux), *Sachtleben*, and *Aldrich* barite (Vinograd et al. 2017) b) of the mechanical mixture of *celestine 99* + *barite 1*, c) experiments with solid solutions $(Ba_{0.01}Sr_{0.99})SO_4$ and $(Ba_{0.03}Sr_{0.97})SO_4$. d, e, f) Temporal evolution of the Ba_{aq} concentrations in the Ra -uptake experiments and g, h, i) in reference experiments without Ra : *Reference barite* (d & g), *reference celestine 99* + *barite 1* (e & h), *reference* $(Ba_{0.01}Sr_{0.99})SO_4$ and *reference* $(Ba_{0.04}Sr_{0.96})SO_4$ (f & i). Lines indicate the equilibrium concentrations calculated with GEMS.

3.2. Evolution of the solid phases

In general, the solids synthesized by the flux method exhibit an irregular shape and morphology, dominated by fractured conchoidal surfaces, thus deviating significantly from the equilibrium morphology, which typically shows characteristic idiomorphic crystal faces. In contrast, the Sachtleben and Aldrich barites used in earlier studies consisted of partially idiomorphic, unbroken particles. Therefore, it could be expected that solids synthesized by the flux method could show a different reactivity.

3.2.1 SEM observations on pure barite in contact with Ra-bearing solution

In the experiment without Ra (*reference barite*), only minor changes in the size and in the surface morphology of barite grains were noted. In contrast, the conchoidal surfaces disappeared in the presence of Ra indicating a continuous transformation from fractured surfaces towards idiomorphic crystal faces.

3.2.2 SEM observations on experiments with the mechanical mixture: Initial phase of recrystallization

In the Ra-free experiment (*reference celestine 99 + barite 1*) no significant changes in the shape of the celestine grains could be seen until day 226 (Fig. 4 a, b). On the contrary, small idiomorphic precipitates ($\sim 3 - 5 \mu\text{m}$) were observed on celestine surfaces already after day 1 in the experiment with the Ra-bearing solution (*celestine 99 + barite 1*). These precipitates contained significant amounts of Ba and Ra in the mole percent range (Fig. 4 g; the EDS spectrum is given in the supplementary materials, Fig. S2). Unfortunately, no primary barite grains were identified in the sampled volume taken from the experiment with the mechanical mixture (*celestine 99 + barite 1*) after day 1, making it impossible to characterize changes in the morphology or in the composition of the barite grains.

After 226 days, the celestine particles in the Ra-free reference experiment (*reference celestine 99 + barite 1*) did not change their morphology, whereas slight changes in the shape of the crystals accompanied by a minor uptake of Sr were observed on the primary barite (Fig. 4 b). In the

394 presence of Ra, the newly formed idiomorphic Ba and Ra rich crystals were still present on the
395 celestine surfaces after 226 days (*celestine 99 + barite 1*) (Fig. 4 h). In addition, the solid sample taken
396 at day 226 contained several former pure barite grains which were partially recrystallized to a ternary
397 (Sr,Ba,Ra)SO₄ solid solution (Fig. 4 e). EDS analyses of the rim indicated a composition of about 1/3
398 Ba, 1/3 Ra and 1/3 Sr (Table S2). Trace amounts of Pb were also detected, most likely stemming from
399 impurities in the used chemicals (99.99+ purity). The analyzed sample contained one broken grain
400 allowing visualization of the core composed of the initial barite and the rim composed of the
401 (Sr,Ba,Ra)SO₄ solid solution. The EDS element distribution across this grain is shown in Figure S3 of
402 the supplements.

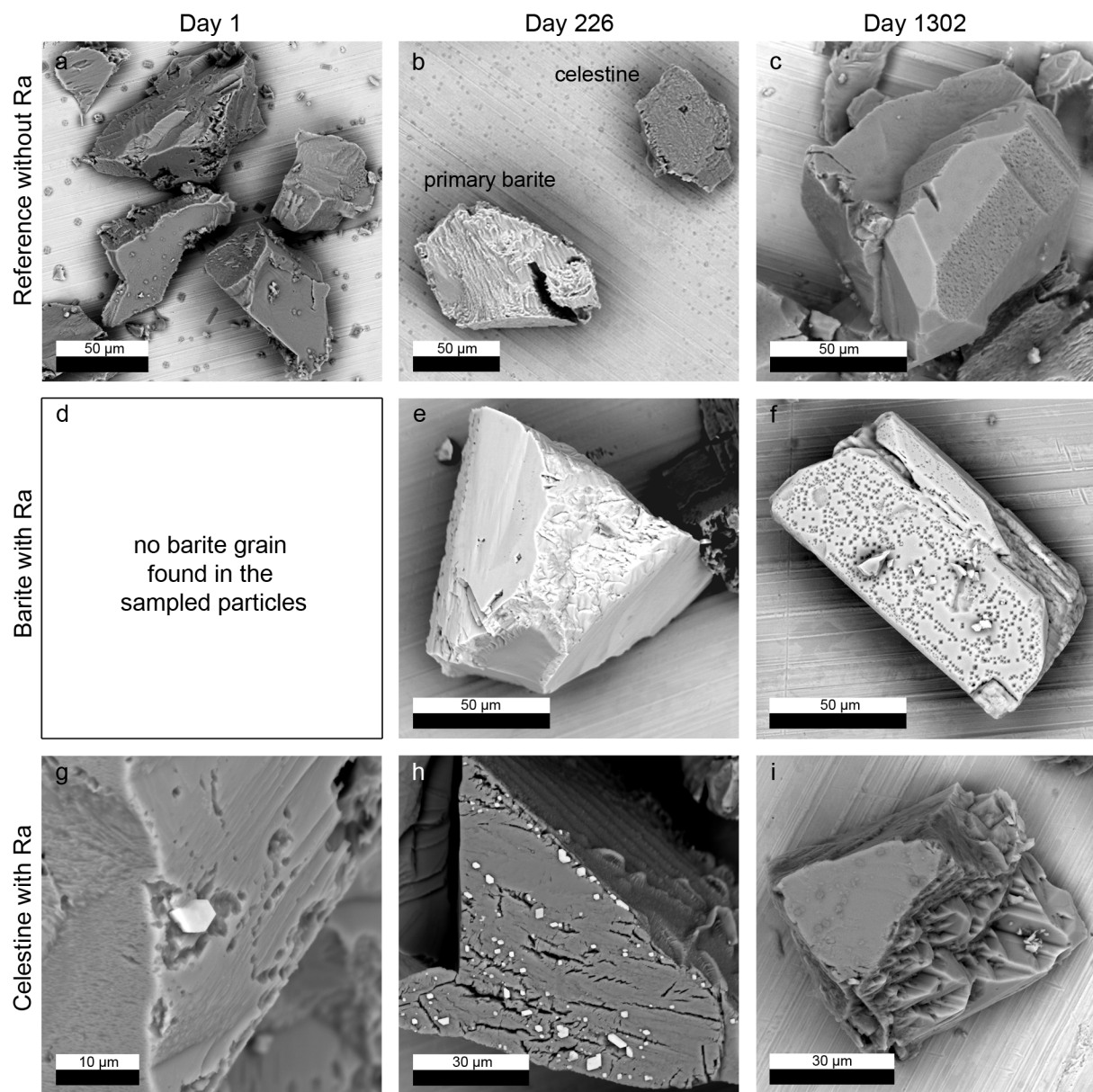


Fig. 4. a-c) Temporal evolution of the solid of the experiment *reference celestine 99 + barite 1* without Ra. d-f) Temporal evolution of primary barite grains in the presence of Ra. g-i) Temporal evolution of primary celestine in contact with Ra.

3.2.3 FIB/SEM and TEM-observations of partially recrystallized barite taken at day 226

A thin lamella was extracted from a primary barite grain (position marked in Fig. S4 a of the supplements). The chemical composition as determined by EDS (particle 2, Table S2) was: Sr: 48.4 at%, Ra: 25.2 at%, Ba: 26.6 at% (mean values). The prepared lamella is displayed in Fig. S4 b. The HAADF STEM imaging of the cross-section lamella clearly showed different signals between the core and the rim region of the particle. A much stronger intensity was obtained in the rim region as shown in Fig. 5. This indicates a significant increase in the average atomic number, assuming a similar sample thickness, coherent crystal structure and orientation between core and rim. Further details were observed in the rim region, which exhibits lamellar-like modulations. These modulations appear along the surface region of the rim (Fig. 5 b), while they were more parallel to the interface at the barite core (Fig. 5 c).

Selected area electron diffraction of the core and rim regions as displayed in Fig. 6 showed a high degree of similarity. Precise analysis of the two patterns yields small deviations: (i) The lattice in the rim region showed a general expansion of 1.0126(3) along the $\langle 100 \rangle$ direction and of 1.0067(3) along the $\langle 0\bar{1}1 \rangle$ direction relative to the barite lattice of the particle core region, where numbers in brackets are estimates of the measurement error for the last digit. (ii) A small relative rotation and angular lattice distortion of about 0.5° was observed between the two patterns, which were recorded under identical imaging conditions.

EDS was performed in the TEM from selected areas of the cross-section sample. The spectra obtained showed a significantly reduced Ba emission in the rim region as well as additional Sr and Ra emissions. Assuming a direct linear relationship between recorded X-ray signal and composition, the reduction of the Ba L intensity corresponds to a fraction of 0.36(1) in the rim composition. This assumption includes that the X-ray signal generation is not affected by a change in diffraction conditions, which seems valid considering the similarity observed in the electron diffraction of Fig. 6.

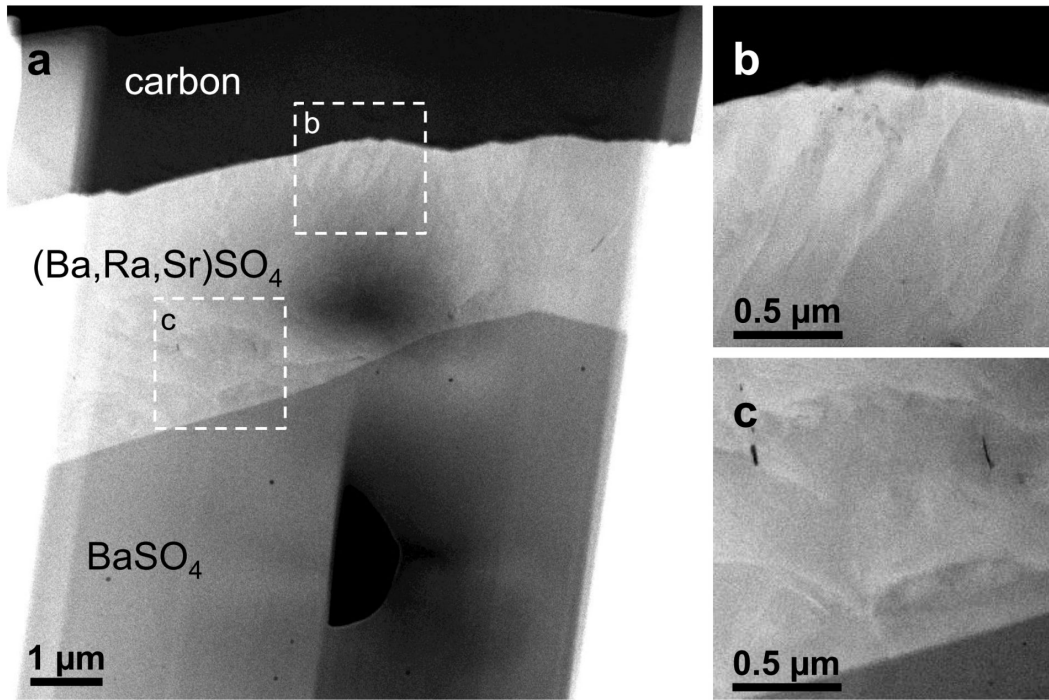


Fig. 5. HAADF STEM images of the cross-section lamella. a) Overview showing the barite core with lower intensity than the (Sr,Ba,Ra)SO₄ rim. Dashed rectangles mark the areas where the enlarged images (b) and (c) were recorded, showing a modulation of the HAADF signal at the surface and the interface, respectively.

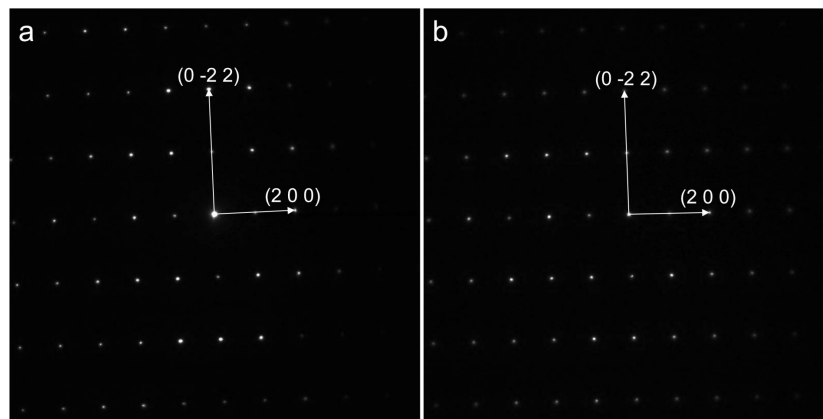


Fig. 6. SAED pattern recorded from (a) the barite region and (b) the rim region of the TEM lamella. The pattern corresponds to a $\{0\ 1\ 1\}$ zone axis orientation. The reciprocal lattice of barite has a length of 0.2796 1/Å for the (2 0 0) vector and of 0.4304 1/Å for the (0 $\bar{2}$ 2) vector (Jacobsen et al. 1998).

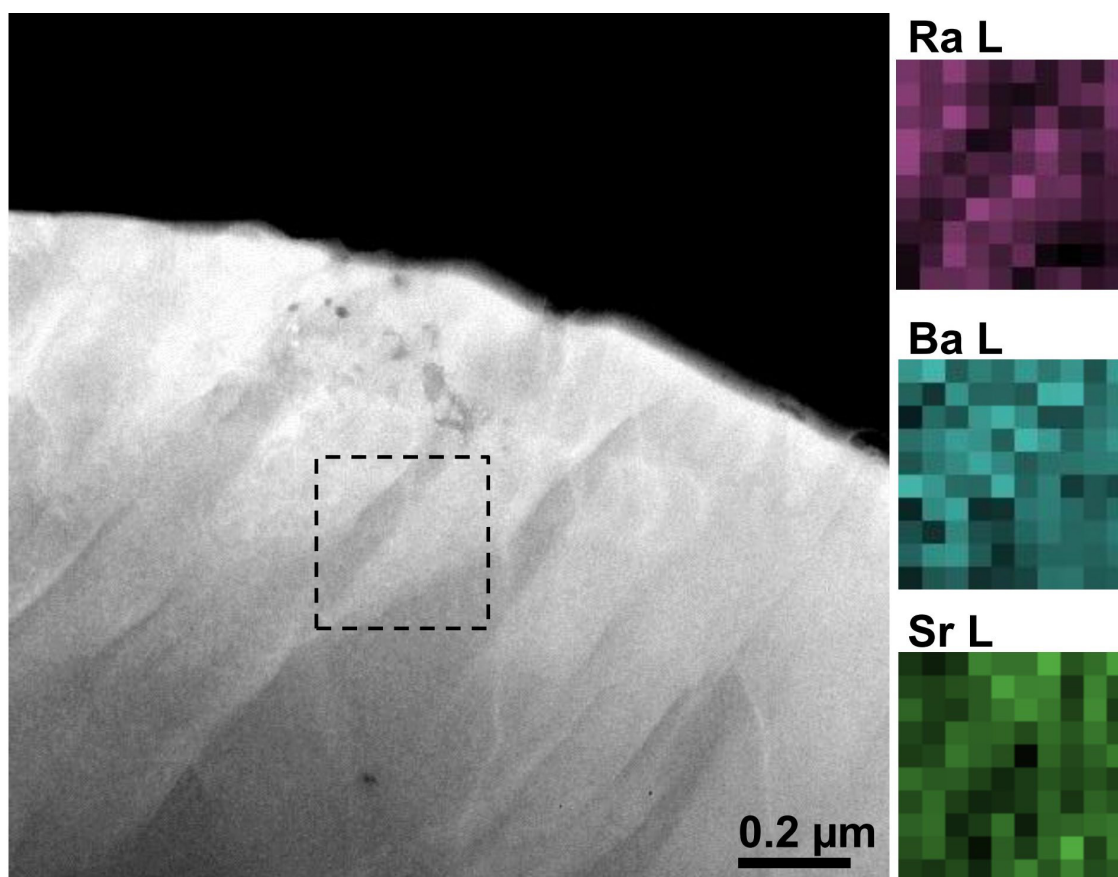


Fig. 7. STEM EDS mapping of the lamellar features observed in the HAADF STEM image (left) close to the particle surface. The elemental maps of the Ra, Ba, and Sr L lines show a similar modulation. The maps of the Ra L and the Sr L signal show an anti-correlation indicating that the modulations are of chemical nature and due to compositional variations of the involved cations.

Additionally, a possible change in X-ray absorption is assumed to be of minor importance for a thin sample as used here. Based on a reference measurement from a perovskite $(\text{Ba}_{0.5}\text{Sr}_{0.5})(\text{Co}_{0.8}\text{Fe}_{0.2})\text{O}_3$ with a known ratio of Ba:Sr = 1 under identical conditions with the same instrument, the Ba:Sr ratio in the rim region was measured with 1.03(2). Further assuming a solid solution, the final composition in rim region is deduced as $(\text{Ba}_{0.36}\text{Sr}_{0.35}\text{Ra}_{0.29})\text{SO}_4$, excluding systematic errors of the measurement, which could have been introduced by deviations from assumptions made. The statistical error of the composition analysis is estimated with 1 %. The results confirm the SEM/EDX measurements.

Variations observed in elemental maps of the Ra, Ba, and Sr L edge EDS signal in the rim region, as displayed in Fig. 7, indicated the presence of local compositional variations including an anti-correlation of the Ra and Sr content. In particular the EDS Ra L signal variations correlate with the HAADF signal variations of the STEM images, i.e. more intense regions in the STEM images contain a higher concentration of Ra and a respectively lower concentration of Sr compared to darker regions. The variations in the Ba map showed no clear spatial correlation to the Ra or the Sr signal.

3.2.4 SEM observations on experiments with the mechanical mixture, approach to equilibrium:

At the end of the Ra-free reference experiment, none of the initial barite grains could be found while newly idiomorphic crystals of $\text{Sr}_{1-x}\text{Ba}_x\text{SO}_4$ were present, with $x = 0.03$ to 0.05 , in addition to the pure celestine (Fig. 4c). In the presence of Ra, between day 226 and day 1302 the small idiomorphic $(\text{Ba,Ra,Sr})\text{SO}_4$ crystals disappeared, while the formation of newly formed crusts was noted at the surfaces of SrSO_4 grains. These contained Ba as detected on a sample taken at day 744 (Figure S5 a, c). Furthermore, in the sample taken at day 744, idiomorphic celestine crystals were observed (Figure S4 b, d). At the end of the experiment, no Ba or Ra could be detected in the Sr-rich phase (Fig. 4 i). The Ba-rich phase (Fig. 4 f) originating from pure barite, contained no detectable amounts of Sr and Ra.

3.2.5 SEM observations on experiments with solid solutions $(\text{Ba}_{0.01}\text{Sr}_{0.99})\text{SO}_4$ and $(\text{Ba}_{0.03}\text{Sr}_{0.97})\text{SO}_4$

The microscopic observations of solids from the two reference experiments with Sr-rich $(\text{Sr,Ba})\text{SO}_4$ solid solutions yielded very similar results (Fig. 8 a - c and Fig. S6 a - c). At day 1 (Fig. 8 a and Fig. S6 a), precipitates of a Ba-rich phase appeared on the primary solid solution grains. At day 226 these initial precipitates disappeared in favor of a surface layer (crust) which was enriched in Ba (Fig. 8 b and Fig. S6 b). At day 1302, the grains sampled from both reference experiments were predominantly characterized by smooth idiomorphic surfaces (Fig. 8 c and Fig. 5 c). No chemical inhomogeneities could be observed by EDS.

Similar observations were made for recrystallization of Sr-rich solid solution in the presence of Ra (experiments $(\text{Ba}_{0.01}\text{Sr}_{0.99})\text{SO}_4$ and $(\text{Ba}_{0.03}\text{Sr}_{0.97})\text{SO}_4$). At day 1, Ra was present in measurable

amounts in the Ba-rich precipitates occurring on the primary solid solution particles (Fig. 8 d and Fig. S6 d). Similarly to the reference experiments, at day 226 the Ba-rich precipitates were dissolved and Ba-rich layers (crusts) were formed on the primary grains (Fig. 8 e and Fig. S6 e). Due to dilution effects Ra could not be detected within these crusts. At the final stage of the experiment, after 1302 days, the idiomorphic features dominated the grains morphology (Fig. 8 f and Fig. S6 f). The chemical composition determined by EDS of the solid solutions at the end of the experiment was $\text{Sr}_{1-x}\text{Ba}_x\text{SO}_4$, with $x = 0.016$ for $(\text{Ba}_{0.01}\text{Sr}_{0.99})\text{SO}_4$ and $x = 0.053$ for $(\text{Ba}_{0.03}\text{Sr}_{0.97})\text{SO}_4$ (Table S3).

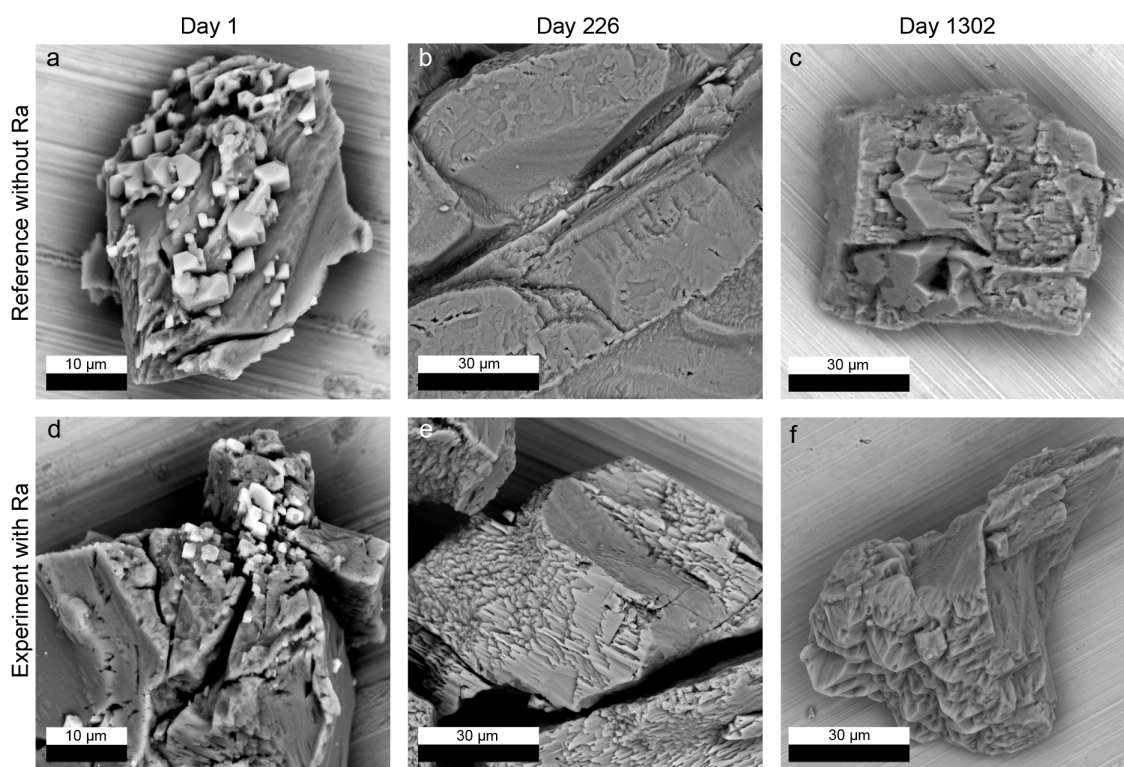


Fig. 8. a-c) Temporal evolution of the solid in the *reference* $(\text{Ba}_{0.03}\text{Sr}_{0.97})\text{SO}_4$ experiment d-f) Temporal evolution of solids in the experiment $(\text{Ba}_{0.03}\text{Sr}_{0.97})\text{SO}_4$ in the presence of Ra.

In summary of the microscopic results, the solids in the experiments with the mechanical mixture and solid solutions changed significantly with time and several metastable phases were observed. Different stages were observed in the Ra-free reference experiment and in the ternary system of the mechanical mixture. While the barite remains stable for a rather long time in the Ra-free experiment, eventually a single phase binary solid-solution $(\text{Ba},\text{Sr})\text{SO}_4$ is formed. The ternary system remains two phase to the very end, with small Ba and Ra-rich precipitates at the surface of the primary celestine

and ternary coatings on the primary barite at the beginning and two distinct Ba or Sr-rich phases at the end. Already after one day, the experiments with the homogenous solid solutions showed a phase separation by the formation of Ba-rich precipitates in the presence of Ra as well as without Ra. These contain considerably amounts of Ra in the case of the ternary system. The Ba-rich precipitates dissolved completely with time and gradually formed crusts on the primary grains, which eventually recrystallized to a homogeneous single phase solid solution. The evolution of the solids is compared to thermodynamic modelling results in section 3.3

3.3. Thermodynamic modelling

3.3.1 Predicted equilibrium states and final experimental conditions

For all experiments, the calculated Ra_{aq} concentrations at equilibrium are slightly higher than the measured concentrations at the end of the experiment (Ra equilibrium concentrations calculated using GEMS in horizontal lines of Fig. 3). Such a deviation was previously noted and discussed in the study of Vinograd et al. 2018b. The calculated Sr_{aq} concentrations in the experiments with the mechanical mixture of *celestine 99 + barite 1* and with the solid solutions $(Ba_{0.01}Sr_{0.99})SO_4$ and $(Ba_{0.03}Sr_{0.97})SO_4$ are in good agreement with the experimental data (Fig. S1 b). For pure barite, the total Ba_{aq} concentrations also match with the simulated values. However, in the case of the mechanical mixture and the solid solutions, in both experiments with and without Ra, there are slight discrepancies between the experimental and simulated Ba_{aq} concentrations. These could indicate that the equilibrium was not reached in these experiments.

The calculated solid compositions at equilibrium are presented in Table 2. In the experiment with pure *barite* in contact with the Ra containing solution, the theoretical equilibrium state corresponds to an almost pure barite with highly diluted Ra concentration. This is in good agreement with our microscopic results at the end of the experiment after 1302 days, where a homogeneous barite is observed, and no significant Ra signal could be measured beyond the detection limits of the EDS instruments. In the case of the experiment with the mechanical mixture *celestine 99 + barite 1*, only one Sr-rich phase is predicted to be stable. This prediction refers to both, the Ra-free reference experiment and to the recrystallization experiment with Ra. However, the microscopic results showed

that two phases were present at the end of both experiments after 1302 days. In the case of the Ra-free reference experiment, two Sr-rich phases were observed: a pure celestine and an idiomorphic Sr-rich $\text{Sr}_{1-x}\text{Ba}_x\text{SO}_4$ solid solution with $x = 0.03$ to 0.05 . In the presence of Ra, a Ba-rich phase remained present together with an almost pure celestine (Fig. 4). The presence of Ra, Sr-rich as well as Ba-rich phases in the experiments stand in contrast to the thermodynamic predictions. This can be caused by an inaccuracy of the thermodynamic data base but also by an insufficient equilibration of the experiment.

Similar to the case of the mechanical mixture, the experiments, in which the starting solid was represented by homogeneous solid solutions, $(\text{Ba}_{0.01}\text{Sr}_{0.99})\text{SO}_4$ and $(\text{Ba}_{0.03}\text{Sr}_{0.97})\text{SO}_4$, are also predicted to equilibrate as single phase assemblages. Our observations are indeed consistent with this prediction, as only one Sr-rich phase was present at the end of both of these experiments (day 1302, Fig. 8 f and Fig. S6 f). However, these solid solutions contained more BaSO_4 than is expected (Table S3). This observation could be very important suggesting that the equilibrium has not been reached in these experiments and that the higher concentrations of Ba_{aq} measured at day 1302 (Fig. 3 f, i) could be maintained via a metastable equilibrium with a Ba-enriched precipitate. As the final Ba_{aq} concentrations were similar in the experiments with the solid solution and with the mechanical mixture, the mechanical mixture experiments also not likely have achieved the equilibrium.

Table 2: Calculated compositions of solid solutions present at equilibrium (X for mole fraction).

Experiment	Composition of solid solution present at equilibrium		
	Sr end member X_{SrSO_4}	Ba end member X_{BaSO_4}	Ra end member X_{RaSO_4}
<i>Barite</i>	-	0.9998	0.0002
<i>Reference celestine 99 + barite 1</i>	0.9918	0.0082	-
<i>Celestine 99 + barite 1</i>	0.9916	0.0082	0.0002
<i>Reference $(\text{Ba}_{0.01}\text{Sr}_{0.99})\text{SO}_4$</i>	0.9934	0.0066	-
<i>$(\text{Ba}_{0.01}\text{Sr}_{0.99})\text{SO}_4$</i>	0.9933	0.0066	0.0002
<i>Reference $(\text{Ba}_{0.03}\text{Sr}_{0.97})\text{SO}_4$</i>	0.9802	0.0198	-
<i>$(\text{Ba}_{0.03}\text{Sr}_{0.97})\text{SO}_4$</i>	0.9800	0.0198	0.0002

3.3.2 Evolution of phases and supersaturation in the reference experiments of $(\text{Sr},\text{Ba})\text{SO}_4 + \text{H}_2\text{O}$ system

As follows from the calculated saturation functions presented in Fig. 9 a, in the reference experiment with the mechanical mixture (*reference celestine 99 + barite 1*) at day 1 the aqueous solution is undersaturated with respect to barite-rich compositions and is supersaturated with respect to celestine-rich compositions. At day 226, the solution is supersaturated with respect to pure celestine and is close to equilibrium with respect to pure barite, while at day 744 the solution is slightly undersaturated with respect to all compositions.

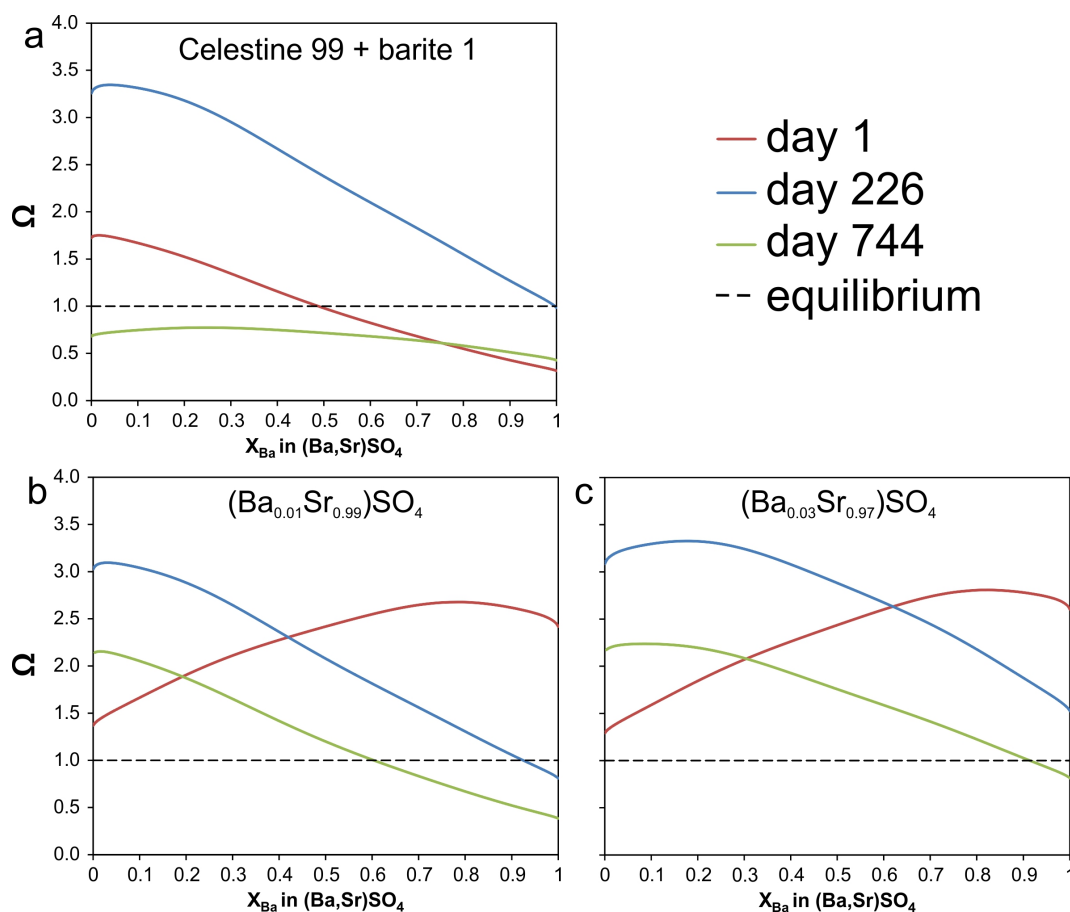


Fig. 9. Temporal evolution of the supersaturation functions (Ω) in experiments without Ra, a) mechanical mixture of *reference celestine 99 + barite 1*, b) *reference $(\text{Ba}_{0.01}\text{Sr}_{0.99})\text{SO}_4$* and c) *reference $(\text{Ba}_{0.03}\text{Sr}_{0.97})\text{SO}_4$* . The supersaturation is calculated from the measured concentrations in an aqueous solution at day 1 (red), day 226 (blue) and day 744 (green) relative to all possible compositions of the solid solution of $(\text{Sr},\text{Ba})\text{SO}_4$. x = mole fraction.

The calculated supersaturation functions are in good agreement with our SEM observations. Our calculations suggest that at day 1 barite-rich compositions are undersaturated. Thus, the few barite crystals present in the mixture should tend to dissolve. Indeed, no newly formed Ba-rich crystals were observed in SEM at day 1. Further, Fig. 4 b shows that at day 226 the few remaining grains of barite were overgrown by a crustal layer which contained a small fraction of SrSO_4 . This observation is reconciled with the relatively high supersaturation calculated for BaSO_4 -rich compositions, suggesting that the crust is likely composed of a relatively Ba-rich solid solution, which is grown epitaxially on the grains of barite. At day 744 our calculations indicate a slight undersaturation with respect to all compositions, suggesting that the approach to equilibrium is a dynamic process, which possibly occurs through several dissolution and re-precipitation stages. The maximum of the supersaturation curve occurs at ~25 at% of BaSO_4 , suggesting that the aqueous solution approaches the equilibrium state, but does not yet match the theoretical composition of the solid.

In the experiments with the single-phase solid solutions without Ra (*reference* $(\text{Ba}_{0.01}\text{Sr}_{0.99})\text{SO}_4$ and *reference* $(\text{Ba}_{0.03}\text{Sr}_{0.97})\text{SO}_4$) after day 1, the aqueous solution was strongly supersaturated with respect to Ba-rich solid solutions (Fig. 9 b, c), suggesting that a Ba-rich phase was able to crystallize even on a structurally misfitting substrate. The supersaturation with respect to barite-rich compositions apparently occurred due to the fast dissolution of the celestine-rich solid solution, which contained a significant amount of BaSO_4 . As the BaSO_4 component dissolved simultaneously with the SrSO_4 component, the concentration of Ba_{aq} increased quite rapidly. Consistently, our SEM observations showed the formation of Ba-rich precipitates with well-shaped faces on top of the primary celestine (Fig. 8 a, d) at day 1.

Similar to the case of the mechanical mixture, in the experiments with the solid solutions the maximum of the supersaturation function at day 226 was shifted significantly to Sr-rich compositions (Fig. 9 a, b). These calculations are in good agreement with the observation that the almost pure barite crystals observed on top of the primary solid solution were converted to a Ba-containing crust which had very little SEM contrast to the primary solid solution and was thus Sr-rich (Fig. 8 b). Furthermore, our calculations show that in the experiments with the solid solutions at day 744 the aqueous solution was still supersaturated with respect to Sr-rich compositions but undersaturated with respect to Ba-rich

compositions, thus providing the possibility for the system to closely move to the predicted homogeneous Sr-rich equilibrium solid solution state. Generally, the supersaturation function calculated at day 744 approximates the equilibrium state much closer than at day 226. Fig. 9 b shows that the maximum of the supersaturation curve moves closer to the theoretical equilibrium composition of a Sr-rich solid solution, while its maximum decreases, thus approaching to the theoretical value of 1. In both reference experiments starting from single-phase (Sr,Ba)SO₄ solid solutions, at day 1302, the SEM observations indicated the formation of newly-formed idiomorphic crystal faces at the surfaces of celestine grains, which implied their further re-equilibration.

Conclusively, after 744 days, and possibly even after 1302 days, the equilibrium was not achieved, both in the experiments with the mechanical mixture (*reference celestine 99 + barite 1*) and in the reference experiments with solid solutions (*reference (Ba_{0.01}Sr_{0.99})SO₄* and *reference (Ba_{0.01}Sr_{0.99})SO₄*). However, all systems demonstrated an approach towards equilibrium. Consistently with this statement, the final concentrations of Ba_{aq} in the long-term Ra-free experiments with the mechanical mixture (*reference celestine 99 + barite 1*) and the solid solution (*reference (Ba_{0.01}Sr_{0.99})SO₄*) approached a similar value of $\sim 2 \cdot 10^{-6}$ mol/L.

3.3.3 Evolution of phases and supersaturation in the ternary (Sr,Ba,Ra)SO₄ + H₂O system

Starting from single-phase solid solutions, the evolution of the Sr_{aq} and Ba_{aq} concentrations in the ternary SS-AS systems was similar to their evolution in experiments without Ra, indicating that the ternary system behavior is largely determined by the behavior of the binary solid solution, which takes up Ra as a trace element. In contrast, in the presence of Ra, the SS-AS system composed initially of two distinct phases behaved differently compared to the Ra-free reference experiment. In the following, the temporal evolution of supersaturation functions (Fig. 10) in the ternary system is discussed in more detail referring to two series of Ra uptake experiments, in which the starting compositions were represented by the mechanical mixture *celestine 99 + barite 1* and by the solid solution (*Ba_{0.01}Sr_{0.99})SO₄*.

In contrast to the reference experiment (*reference celestine 99 + barite 1*), in the experiment with Ra at day 1 the aqueous phase was supersaturated not only with respect to Ba-rich compositions (Fig.

10 a), but also with respect to a wide area of ternary compositions extending to Ra contents of up to 75 %. This difference in supersaturation conditions correlates well with our SEM observations of small Ba- and Ra-rich crystals with well-developed crystal faces formed on the surfaces of the celestine crystals (Fig. 4 g). The same figure shows various signs of partial dissolution of the latter crystals. Ra naturally accumulates in the minor newly-formed Ba-rich phase as also discussed in Vinograd et al. 2018b. These crystals appear to remain stable up to day 226 and, possibly, longer. At day 226 the composition of the aqueous solution is supersaturated with respect to Sr-rich compositions and is slightly undersaturated with respect to the intermediate ternary compositions. The rims on the primary barites sampled at day 226 and discussed in detail in 3.2.2 and 3.2.3, could be the relicts of the earlier phase of recrystallization. The observed intermediated ternary compositions of the rims can be rationalized noting that they fall into the “low misfit area” in the ternary plot, where the misfit function Q is defined relative to pure barite. The lowest structural misfit corresponds to compositions with the Sr/Ra ratios of ~ 0.4 . The equal misfit lines are shown in Fig. 10 a, c, e. At the beginning of the experiment, the aqueous solution was supersaturated with respect to a wide range of intermediate ternary compositions providing the necessary condition for the rim deposition (Fig. 10 a). At day 744 the area on the ternary plot, over which the aqueous phase is supersaturated further shrinks to the very vicinity of the celestine corner. At the same time, it remains only slightly undersaturated at the barite corner. This shift generally reflects the tendency of the system to move to the thermodynamic equilibrium, and also explains why the barite phase is still present at the end of the mechanical mixture experiments. At day 1302 no Ra-rich phases could be seen in our SEM-observations, suggesting that Ra is more homogeneously distributed within the celestine- and barite-rich phases. The surfaces of the original celestine crystals reveal newly formed faces, reflecting their partial or complete recrystallization. This is in good agreement with the calculated supersaturation function (Fig. 10 e) which at day 744 indicates a strong undersaturation in all areas except the Ba- and Sr-rich corners. Since both Ba- and Sr-rich compositions appear to be close to equilibrium, a metastable two-phase system seems to have very little driving force to re-equilibrate to the thermodynamically predicted one-phase system. However, it remains unclear due to the low Ra-concentrations resulting from total equilibration of all solid or significant amounts of solid, which solid has taken up most of the Ra.

From the thermodynamic point of view, if the two phases are at equilibrium, the activity of RaSO_4 in both phases should be similarly suggesting that the total amount of Ra may be approximately equally split between the two phases. Sr-rich solid solution would be likely host for Ra.

In the case of the experiment with the $(\text{Ba}_{0.01}\text{Sr}_{0.99})\text{SO}_4$ solid solution put in contact with the Ra-bearing aqueous solution the supersaturation functions differ from the case of the mechanical mixture, particularly at day 1 (Fig. 10 b), predicting the formation of more Ba-rich and less Ra-rich precipitates. In agreement with the calculated supersaturation, SEM observations showed newly precipitated Ba- and Ra-rich crystals on the primary solid solution surfaces. At a later stage of this experiment, at day 226, the composition of the aqueous solution shifted towards more Sr-rich compositions (Fig. 10 d). Accordingly, no Ba-rich crystals were observed on the primary celestine surfaces. Instead, new crusts appeared on the surfaces. These crusts have very little SEM contrast to the primary solid solution suggesting a high Sr content. At day 744, the region of strong undersaturation stretches almost to the complete ternary plot, leaving only the Sr-rich corner in slight supersaturation (Fig. 10 f). This transition correlates with the SEM-EDX results obtained for the samples taken after day 1302. The final assemblage occurs as a homogenous single-phase solid solution, whose Ba/Sr ratio is very close to the thermodynamically predicted composition.

Our experiments and modelling results thus suggest that rather high degrees of non-equilibrium remain in the system after day 226 and a decrease in the supersaturation, which is consistent with the approach to true equilibrium, occurs only after about two years. This is in agreement with the results of Felmy et al. (1993) who studied the solubility of $(\text{Ba,Sr})\text{SO}_4$ precipitates of a wide range of compositions in aqueous solutions. Felmy et al. (1993) noted that a reversible equilibrium with the aqueous solution could be obtained only at the time scale of about 1 year. Consistently with the present results, Felmy et al. (1993) observed a significant increase in Ba_{aq} concentration in short-term experiments, which was leveled out only after 315 days. This shows that in the both studies the equilibration starts with the congruent dissolution of the solid solution, what causes a release of a large amount of Ba in the aqueous phase. A similar initial increase in Ba_{aq} was also observed in the system of $(\text{Ba,Pb})\text{SO}_4$ studied by Kornicker et al. (1991). Within the initial process of congruent dissolution the aqueous solution quickly becomes supersaturated with respect to the less soluble component, i.e.

BaSO₄, causing the appearance of early Ba-rich precipitates. Felmy et al. (1993) noted that their solubility data were inconsistent with the assumption of a stoichiometric saturation involving a single solid solution phase. They suggested that a nearly pure secondary BaSO₄ was immediately formed and remained in the system throughout the experiment controlling the aqueous concentration of Ba. Our study offers an important modification to the two-phase model of Felmy et al. (1993) as we could show that the Ba-rich precipitates did not persist throughout the experiment. Our detailed SEM study showed that the early Ba-rich phases were replaced after 226 days by more Sr-rich precipitates, while the longest-term experiments resulted in the formation of Sr-rich crystals whose composition approached the theoretical prediction. Our results suggest that the rapid formation of Ba-rich precipitates causes a depletion of Ba_{aq} concentration, which, in turn, causes the aqueous phase to become supersaturated with respect to more Sr-rich compositions. The subsequent crystallization of more Sr-rich, but still Ba-rich precipitates requires a further consumption of Ba_{aq}, what, in turn, drives the dissolution of the early Ba-rich crystals. The predicted temporal shift of the maximum of the supersaturation function from Ba-rich to more Sr-rich compositions provides the mechanism of a gradual approach of the system to the equilibrium state.

Mechanical mixture

Solid solution

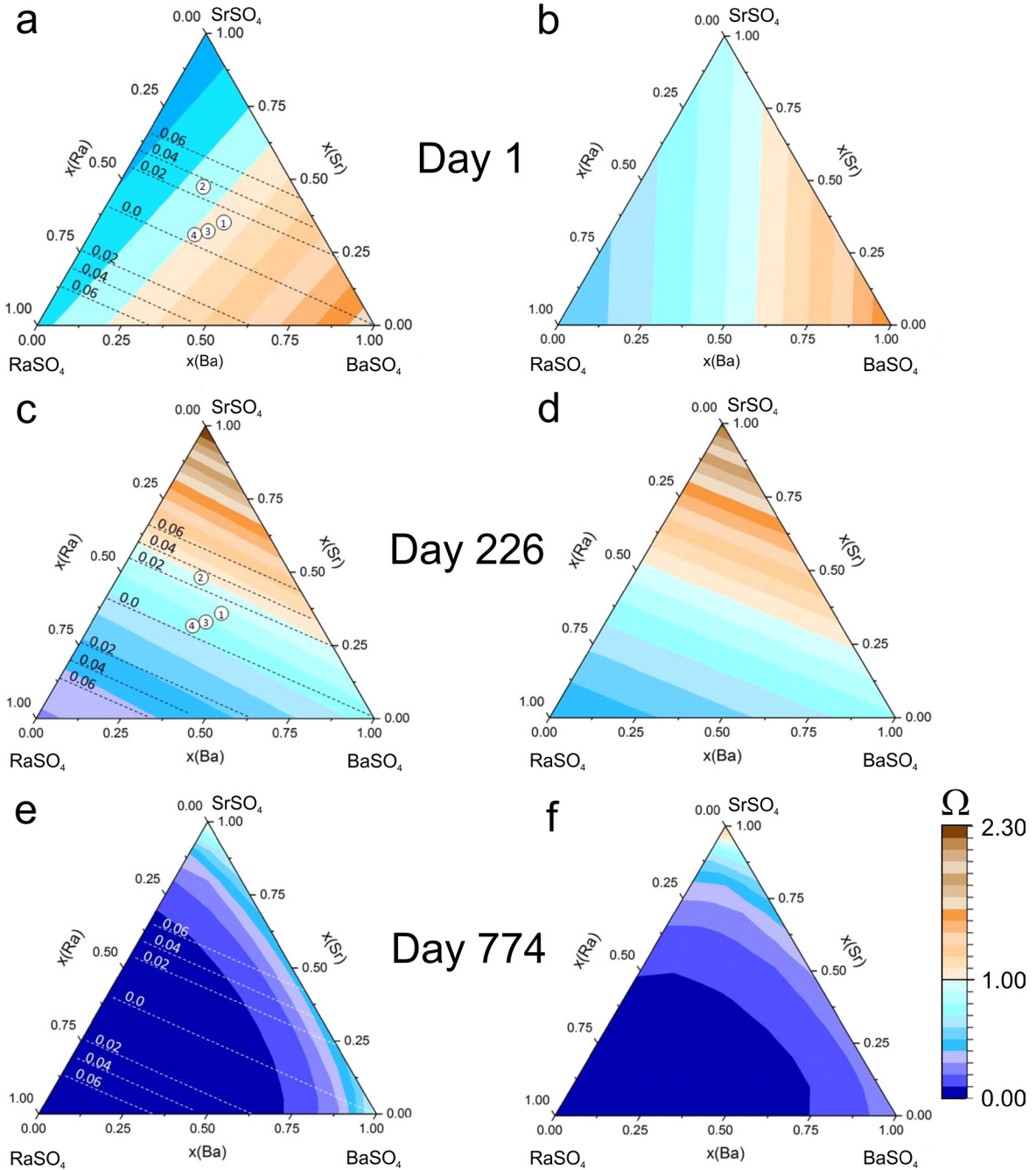


Fig. 10. Supersaturation of the aqueous phase relative to the ternary solid solution in the experiments with the mechanical mixture of *celestine 99 + barite 1* (a, c, e) and the solid solution $(Ba_{0.01}Sr_{0.99})SO_4$ (b, d, f) after day 1 (a, b), day 226 (c, d) and day 744 (e, f). The intensities of blue and brown colors correlate with the degree of undersaturation and supersaturation, respectively. White circles denote the composition of the crustal layer grown on top of primary barite grains measured after day 226 of the mechanical mixture. The dashed lines (a, c, e) illustrate the misfit Q of the ternary solid solution phase relative to pure barite.

4 Summary and conclusions

The primary aims of this combined experimental and modelling study were to measure the Ra-uptake at Sr-rich compositions within the ternary SS-AS system (Sr,Ba,Ra)SO₄ at 90 °C and to compare the results with thermodynamic predictions. An essential experimental result is that the Ra_{aq} concentration has decreased by more than one order of magnitude. The measured decrease is smaller than that observed in the experiments with pure barite but is nevertheless significant. The final Ra_{aq} concentration of $\sim 2.0 \cdot 10^{-7}$ mol/L is very close to the predicted concentration at the thermodynamic equilibrium at 90 °C in a system composed of 5 g/L of celestine-rich solid solution. This agreement implies that the available thermodynamic database is sufficiently robust for modelling of systems, in which the Ra-uptake is controlled by sulfates containing variable amounts of barite and celestine. This conclusion is important in the discussion of nuclear waste disposal scenarios, which are concerned with a possible interaction of Ra-contaminated ground waters with host rocks containing barite-type solid solutions.

The re-equilibration of the ternary SS-AS reveals itself as a complex dynamic process, involving the precipitation and dissolution of various secondary metastable phases and the corresponding temporal changes in the composition of the aqueous solution. Supersaturation functions appear to be particularly instrumental in linking the evolution of the solid precipitates to the evolution of the aqueous phase. The calculated functions for the binary and ternary SS-AS systems permitted a straightforward interpretation of our experimental SEM-EDX results. This shows that the thermodynamic data base revised in the earlier studies (Vinograd et al., 2018a,b) provides a sufficiently accurate tool not only for predicting plausible thermodynamic equilibrium states, but also for understanding the mechanisms by which the system evolves towards the final equilibrium from the starting non-equilibrium experimental conditions. For the first time, the existence of a wide range of intermediate, metastable ternary (Sr,Ba,Ra)SO₄ solid solution compositions was observed. It appears that in a SS-AS system the composition of the solid phase does not always take the shortest path in its evolution from the starting to the final equilibrium composition. The compositions of precipitates at intermediate stages may differ quite drastically both from the initial and the end points. The formation of these metastable solid solutions in the short-term experiments provided for the first time a

possibility of the structural investigation of the ternary phase, which is nearly equally composed of BaSO_4 , SrSO_4 and RaSO_4 components. The combination of FIB, SEM and TEM investigations has shown that the average structural parameters of the rim are very similar to that of the barite core. This agreement suggests that the particular choice made by the system in favor of this particular ternary composition, has been driven by the combination of a minimization of the structural mismatch allowing for the coherent growth on the barite surface and supersaturation of the newly formed phase.

Different initial phase associations provided different final phase associations. In the case of the mechanical mixture of 99 % of celestine and 1 % of barite in Ra-bearing solution the final state was represented by a two-phase association of a newly formed celestine and barite, while in the case of the solid solution of identical composition, $(\text{Ba}_{0.01}\text{Sr}_{0.99})\text{SO}_4$, only a single Sr-rich phase was formed. Although our equilibrium thermodynamic calculations are consistent with the single-phase final assemblage (Table 3), the two-phase association found in the experiments with the mechanical mixture may indicate that at 90°C the studied system of $(\text{Ba}_{0.01}\text{Sr}_{0.99})\text{SO}_4 + \text{H}_2\text{O}$ is close to be able to phase separate. Indeed, as discussed by Vinograd et al. 2018b, the addition of RaSO_4 to the binary $(\text{Ba,Sr})\text{SO}_4$ solid solution increases its tendency to phase separate. On the one hand, the addition of Ra destabilizes the Sr-rich phase due to a very large value of the W_{SrRa} parameter. On the other hand, the addition of Ra to the Ba-rich phase does not cost much of enthalpy because of the small value of the W_{BaRa} parameter. Thus, even at a reasonably small total concentration of RaSO_4 in the system, the phase separation may become the thermodynamically preferred state. Although the observation of different final assemblages in experiments with the same total chemical composition can formally be considered as a proof of the absence of the thermodynamic equilibrium, the similarity of the final Ra_{aq} and Ba_{aq} concentrations in the experiments on Ra uptake in the systems composed of the mechanical mixture of *celestine 99 + barite 1* and of the homogeneous $(\text{Ba}_{0.01}\text{Sr}_{0.99})\text{SO}_4$ solid solution (Fig. 3) suggests that the both systems deviated only marginally from the true equilibrium at 90 °C.

759 **Acknowledgements**

760 The research leading to these results has received partial funding from the German Federal Ministry of
761 Education and Research (BMBF) ImmoRad project (project number 02NUK019C) and ThermAc
762 project (project number 02NUK039D). We are grateful to F. Sadowski, C. Kalitz, K. Dahmen, R.
763 Engelmann, G. Deissmann and G. Modolo for their support. We thank Dr. D. Kulik (PSI, Switzerland)
764 for discussions and supporting the thermodynamic calculations (GEMS). Prof. Dr. Th. Nagel (former
765 Bonn University, Germany now University Aarhus, Denmark) is acknowledged for electron
766 microprobe measurements of the synthesized solid solutions.

767

768 **Appendix**

769 **Table A.1:** Temporal evolution of the aqueous Ra and Ba concentrations of experiments with pure
770 *barite*.

Experiment	Ra concentration (mol/L)	Ba concentration (mol/L)	
	Barite	Barite	Reference Barite
Day			
0	5.00E-06		
1	3.49E-06	3.90E-05	4.91E-05
3	2.21E-06	4.19E-05	4.80E-05
8	3.87E-07	4.08E-05	4.33E-05
15	9.61E-08	4.17E-05	4.40E-05
22	5.44E-08	4.23E-05	4.71E-05
29	3.54E-08	3.81E-05	4.72E-05
43	3.44E-08	4.11E-05	4.42E-05
57	2.65E-08	3.70E-05	4.05E-05
71	2.25E-08	3.51E-05	4.82E-05
99	2.37E-08	4.09E-05	4.93E-05
134	2.41E-08	3.56E-05	4.66E-05
165	2.74E-08	3.80E-05	4.57E-05
226	2.47E-08	3.94E-05	4.42E-05
295	1.51E-08	4.57E-05	5.17E-05
405	2.02E-08	4.24E-05	5.38E-05
512	1.60E-08	3.92E-05	5.69E-05
601	1.61E-08	4.22E-05	5.64E-05
744	1.68E-08	4.34E-05	6.86E-05
828	1.02E-08		
1022	7.49E-09		
1085	1.25E-08		
1302	1.00E-08		

771

772

Table A.2: Temporal evolution of the aqueous Ra, Ba, and Sr concentration of experiments with a mechanical mixture of *celestine 99 + barite 1* with 5 g/L at 90 °C and corresponding reference experiments without Ra.

Experiment	Ra concentration (mol/L)	Ba concentration (mol/L)		Sr concentration (mol/L)	
	Celestine 99 + barite 1	Celestine 99 + barite 1	Reference celestine 99 + barite 1	Celestine 99 + barite 1	Reference celestine 99 + barite 1
Day					
1	4.60E-06	1.00E-05	9.98E-07	9.27E-04	1.45E-03
3	3.19E-06	8.48E-06	1.06E-06	1.15E-03	1.57E-03
8	2.66E-06	6.01E-06	1.25E-06	1.00E-03	1.57E-03
15	2.55E-06	6.04E-06	1.47E-06	1.12E-03	1.58E-03
22	2.36E-06	4.85E-06	1.34E-06	1.16E-03	1.55E-03
29	2.26E-06	3.47E-06	1.46E-06	1.12E-03	1.54E-03
43	2.76E-06	3.09E-06	1.73E-06	1.13E-03	1.58E-03
57	2.92E-06	2.91E-06	1.91E-06	1.15E-03	1.53E-03
71	3.18E-06	3.05E-06	1.98E-06	1.18E-03	1.60E-03
99	3.51E-06	2.54E-06	1.96E-06	1.14E-03	1.60E-03
134	3.65E-06	2.45E-06	1.35E-06	1.61E-03	2.03E-03
226	8.77E-07	2.67E-06	2.37E-06	1.75E-03	2.04E-03
295	3.15E-06	2.09E-06	1.37E-06	1.60E-03	2.12E-03
405	2.75E-07	1.63E-06	1.44E-06	1.62E-03	1.95E-03
512	3.81E-07	4.81E-06	2.09E-06	1.29E-03	1.59E-03
601	1.07E-07	3.04E-06	4.51E-07	1.10E-03	1.75E-03
744	1.41E-07	3.84E-06	2.05E-06	1.13E-03	8.89E-04
828	1.01E-07				
1022	2.20E-07				
1085	9.93E-08				
1302	1.67E-07				

778 **Table A.3:** Temporal evolution of the aqueous Ra concentrations of experiments with solid solutions
779 $(Ba_{0.01}Sr_{0.99})SO_4$ and $(Ba_{0.03}Sr_{0.97})SO_4$.

Experiment	Ra concentration (mol/L)	
	$(Ba_{0.01}Sr_{0.99})SO_4$	$(Ba_{0.03}Sr_{0.97})SO_4$
Day		
1	2.45E-06	1.80E-06
3	2.11E-06	1.35E-06
8	2.02E-06	1.17E-06
15	2.39E-06	1.47E-06
22	2.95E-06	1.37E-06
29	3.06E-06	1.98E-06
43	3.16E-06	2.40E-06
57	2.94E-06	2.12E-06
71	2.77E-06	2.25E-06
99	2.45E-06	2.21E-06
134	2.19E-06	1.92E-06
169	1.97E-06	1.38E-06
226	1.31E-06	1.83E-07
295	8.91E-07	2.37E-07
405	3.25E-07	1.79E-07
512	3.74E-07	2.42E-07
601	2.08E-07	1.68E-07
744	1.43E-07	9.39E-08
828	2.34E-07	1.00E-07
1022	9.38E-08	1.35E-07
1085	1.03E-07	1.30E-07
1302	1.62E-07	1.83E-07

780

781

782

Table A.4: Temporal evolution of the aqueous Ba and Sr concentrations of experiments with solid solutions $(Ba_{0.01}Sr_{0.99})SO_4$ and $(Ba_{0.03}Sr_{0.97})SO_4$.

Experiment	Ba concentration (mol/L)			
	$(Ba_{0.01}Sr_{0.99})SO_4$	$(Ba_{0.03}Sr_{0.97})SO_4$	Reference $(Ba_{0.01}Sr_{0.99})SO_4$	Reference $(Ba_{0.03}Sr_{0.97})SO_4$
Day				
1	8.77E-06	8.37E-06	8.45E-06	9.34E-06
3	7.30E-06	7.40E-06	9.21E-06	1.08E-05
8	4.87E-06	5.28E-06	8.13E-06	6.90E-06
15	4.22E-06	4.67E-06	8.26E-06	6.24E-06
22	3.25E-06	4.22E-06	7.67E-06	5.91E-06
29	3.09E-06	3.98E-06	7.82E-06	5.90E-06
43	2.75E-06	3.68E-06	7.69E-06	4.78E-06
57	3.09E-06	3.89E-06	5.56E-06	4.21E-06
71	3.28E-06	4.20E-06	4.89E-06	4.24E-06
99	2.77E-06	3.86E-06	3.71E-06	3.92E-06
134	3.25E-06	4.02E-06	2.72E-06	4.00E-06
169	2.56E-06	3.85E-06	3.07E-06	3.56E-06
225	2.85E-06	3.95E-06	2.01E-06	3.76E-06
295	3.08E-06	3.38E-06	1.56E-06	3.53E-06
405	1.57E-06	2.88E-06	1.00E-06	2.39E-06
512	1.70E-06	3.79E-06	1.27E-06	3.15E-06
601	1.70E-06	3.08E-06	1.13E-06	2.59E-06
744	1.38E-06	3.60E-06	1.11E-06	2.34E-06

787 **Table A.5:** Temporal evolution of the aqueous Sr concentrations of experiments with solid solutions
788 $(Ba_{0.01}Sr_{0.99})SO_4$ and $(Ba_{0.03}Sr_{0.97})SO_4$.

Experiment	Sr concentration (mol/L)			
	$(Ba_{0.01}Sr_{0.99})SO_4$	$(Ba_{0.03}Sr_{0.97})SO_4$	Reference $(Ba_{0.01}Sr_{0.99})SO_4$	Reference $(Ba_{0.03}Sr_{0.97})SO_4$
Day				
1	1.02E-03	9.75E-04	1.28E-03	1.24E-03
3	1.11E-03	1.03E-03	1.27E-03	1.80E-03
8	1.11E-03	1.07E-03	1.27E-03	1.27E-03
15	1.11E-03	1.06E-03	1.35E-03	1.34E-03
22	1.08E-03	1.08E-03	1.30E-03	1.33E-03
29	1.13E-03	1.08E-03	1.30E-03	1.35E-03
43	1.11E-03	1.16E-03	1.41E-03	1.36E-03
57	1.11E-03	1.08E-03	1.37E-03	1.39E-03
71	1.17E-03	1.12E-03	1.41E-03	1.48E-03
99	1.09E-03	1.03E-03	1.41E-03	1.36E-03
134	1.64E-03	1.65E-03	1.92E-03	1.91E-03
169	1.65E-03	1.67E-03	2.00E-03	1.94E-03
225	1.70E-03	1.67E-03	1.96E-03	1.98E-03
295	1.64E-03	1.61E-03	1.96E-03	1.96E-03
405	1.68E-03	1.68E-03	1.95E-03	6.76E-04
512	1.21E-03	1.14E-03	1.56E-03	1.54E-03
601	1.23E-03	1.19E-03	1.63E-03	1.52E-03
744	1.26E-03	1.20E-03	1.62E-03	1.63E-03

789
790

791 **References**

- 792 Brandt, F., Curti, E., Klinkenberg, M., Rozov, K., Bosbach, D., 2015. Replacement of barite by a
793 (Ba,Ra)SO₄ solid solution at close-to-equilibrium conditions: A combined experimental and
794 theoretical study. *Geochim. Cosmochim. Acta* 155, 1–15.
- 795 Bosbach D., Boettle M., Metz V., 2010. Experimental study on Ra²⁺ uptake by barite (BaSO₄). SKB
796 Technical Report TR-10- 43. Stockholm, Sweden.
- 797 Bruno, J., Bosbach, D., Kulik, D., Navrotsky, A., 2007. Chemical thermodynamics of solid solutions
798 of interest in nuclear waste management: a state-of-the-art report, Development.
- 799 Curti, E., Fujiwara, K., Iijima, K., Tits, J., Cuesta, C., Kitamura, A., Glaus, M. a., Müller, W., 2010.
800 Radium uptake during barite recrystallization at 23±2 °C as a function of solution composition:
801 An experimental ¹³³Ba and ²²⁶Ra tracer study. *Geochim. Cosmochim. Acta* 74, 3553–3570.
- 802 Ewing, R. C., Whittleston, R. A., Yardley, B. W., 2016. Geological disposal of nuclear waste: a
803 primer: *Elements* 12 (4), 233-237.
- 804 Felmy, A.R., Rai, D., Moore, D.A., 1993. The solubility of (Ba,Sr)SO₄ precipitates: Thermodynamic
805 equilibrium and reaction path analysis. *Geochim. Cosmochim. Acta* 57(18), 4345-4363.
- 806 Grandia, F., Merino, J., Bruno, J., 2008. Assessment of the radium-barium co-precipitation and its
807 potential influence on the solubility of Ra in the near-field, SKB Technical Report TR-08-07.
808 Stockholm, Sweden.
- 809 Heberling, F., Metz, V., Böttle, M., Curti, E., Geckeis, H., 2018. Barite recrystallization in the
810 presence of ²²⁶Ra and ¹³³Ba. *Geochim. Cosmochim. Acta* 232, 124-139.
- 811 Helgeson, H.C., Kirkham, D.H., Flowers, G.C., 1981. Theoretical prediction of the thermodynamic
812 behavior of aqueous electrolytes by high pressures and temperatures; IV, Calculation of activity
813 coefficients, osmotic coefficients, and apparent molal and standard and relative partial molal
814 properties to 600 degrees C and 5 kb. *Am. J. Sci.* 281, 1249–1516.
- 815 Hummel, W., Berner, U., Curti, E., Pearson, F.J., Thoenen, T., 2002. Nagra / PSI Chemical
816 Thermodynamic Data Base 01/01; Nagra technical report 02-16.
- 817 Jacobsen, S.D., Smyth, J.R., Swope, R.J., Downs, R.T., 1998. Rigid-body character of the SO₄ groups
818 in celestine, anglesite and barite. *Can. Mineral.*
- 819 Johnson, J.W., Oelkers, E.H., Helgeson, H.C., 1992. SUPCRT92: A software package for calculating
820 the standard molal thermodynamic properties of minerals, gases, aqueous species, and reactions
821 from 1 to 5000 bar and 0 to 1000 °C. *Computat. Geosci.*, 18(7), 899-947.
- 822 Klinkenberg, M., Brandt, F., Breuer, U., Bosbach, D., 2014. Uptake of Ra during the recrystallization
823 of barite: A microscopic and time of flight-secondary ion mass spectrometry study. *Environ. Sci.*
824 *Technol.* 48, 6620–6627.
- 825 Kornicker, W.A., Presta, P.A., Paige, C.R., Johnson, D.M., Hileman, O.E., Snodgrass, W.J., 1991. The
826 aqueous dissolution kinetics of the barium/lead sulfate solid solution series at 25 and 60°C,
827 *Geochim. Cosmochim. Acta* 55(12), 3531-3541.

- 828 Kulik, D.A., Berner, U., Curti, E., March 2004. Modelling chemical equilibrium partitioning with the
829 GEMS-PSI code. In: Smith, B., Gschwend, B. (Eds.), PSI Scientific Report 2003/Volume IV,
830 Nuclear Energy and Safety. Paul Scherrer Institute, Villigen, Switzerland, pp. 109–122 (ISSN
831 1423-7334).
- 832 Kulik, D.A., Wagner, T., Dmytrieva, S. V, Kosakowski, G., Hingerl, F.F., Chudnenko, K. V, Berner,
833 U.R., 2013. GEM-Selektor geochemical modeling package: revised algorithm and GEMS3K
834 numerical kernel for coupled simulation codes. *Comput. Geosci.* 17, 1–24.
- 835 Langmuir, D., Riese, A., 1985. The thermodynamic properties of radium. *Geochim. Cosmochim. Acta*
836 49, 1593–1601.
- 837 Luysberg, M., Heggen, M., Tillmann, K., 2016. FEI Tecnai G2 F20. J. large-scale Res. Facil. JLSRF
838 2, A77.
- 839 NAGRA, 2014. Technischer Bericht NTW 14-03. Charakteristische Dosisintervalle und Unterlagen
840 zur Bewertung der Barrierensysteme. Wettingen, Switzerland.
- 841 Patel, A.R., Bhat, H.L., 1971. Growth of strontium sulphate single crystals by chemically reacted flux
842 method and their dislocation configuration. *J. Cryst. Growth* 8, 153–156.
- 843 Patel, A.R., Koshy, J., 1968. Growth of barium sulphate single crystals by chemically reacted flux
844 method. *J. Cryst. Growth* 2, 128–130.
- 845 Pennycook, S.J., 1989. Z-contrast stem for materials science. *Ultramicroscopy* 30, 58–69.
- 846 Pina, C.M., Enders, M., Putnis, A., 2000. The composition of solid solutions crystallising from
847 aqueous solutions: the influence of supersaturation and growth mechanisms. *Chem. Geol.* 168,
848 195–210.
- 849 Prieto, M., Fernández-Díaz, L., López-Andrés, S., 1991. Spatial and evolutionary aspects of nucleation
850 in diffusing-reacting systems. *J. Cryst. Growth* 108, 770–778.
- 851 Prieto, M., Putnis, A., Fernandez-Díaz, L., 1993. Crystallization of solid solutions from aqueous
852 solutions in a porous medium: zoning in (Ba,Sr)SO₄. *Geol. Mag.* 130, 289.
- 853 SKB, 2011. Long-term safety for the final repository of spent nuclear fuel at Forsmark Main report of
854 the Sr-site project I-III. Stockholm, Sweden.
- 855 Thoenen, T., Hummel, W., Berner, U., Curti, E., 2014. The PSI/Nagra Chemical Thermodynamic
856 Database 12/07. PSI Bericht Nr. 14-04, ISSN 1019–0643
- 857 Vinograd, V.L., Brandt, F., Rozov, K., Klinkenberg, M., Refson, K., Winkler, B., Bosbach, D., 2013.
858 Solid-aqueous equilibrium in the BaSO₄-RaSO₄-H₂O system: First-principles calculations and a
859 thermodynamic assessment. *Geochim. Cosmochim. Acta* 122, 398–417.
- 860 Vinograd, V.L., Kulik, D.A., Brandt, F., Klinkenberg, M., Weber, J., Winkler, B., Bosbach, D., 2018a.
861 Thermodynamics of the solid solution - Aqueous solution system (Ba,Sr,Ra)SO₄ + H₂O: I. The
862 effect of strontium content on radium uptake by barite. *Appl. Geochemistry* 89, 59–74.
- 863 Vinograd, V.L., Kulik, D.A., Brandt, F., Klinkenberg, M., Weber, J., Winkler, B., Bosbach, D., 2018b.
864 Thermodynamics of the solid solution - Aqueous solution system (Ba,Sr,Ra)SO₄ + H₂O: II.
865 Radium retention in barite-type minerals at elevated temperatures. *Appl. Geochemistry*, 93, 190-
866 208.

- 867 Wagner, T., Kulik, D.A., Hingerl, F.F., Dmytrieva, S. V, 2012. GEM-Selektor geochemical modeling
868 package: TSolMod library and data interface for multicomponent phase models. *Can. Mineral.*
869 50, 701–723.
- 870 Weber, J., Barthel, J., Brandt, F., Klinkenberg, M., Breuer, U., Kruth, M., Bosbach, D., 2016. Nano-
871 structural features of barite crystals observed by electron microscopy and atom probe
872 tomography. *Chem. Geol.* 424, 51–59.
- 873 Weber, J., Barthel, J., Klinkenberg, M., Bosbach, D., Kruth, M., Brandt, F., 2017. Retention of ^{226}Ra
874 by barite: The role of internal porosity. *Chem. Geol.* 466, 722–732.
- 875 Weigel, F., Trinkl, A., 1967. Zur Kristallchemie des Radiums I. Die Halogenide des Radiums.
876 *Radiochim. Acta* 9, 36–41.